

Full length article

# Analytical modeling and characterization of ring beam profiles for high-power lasers used in industrial manufacturing

Francesco Galbusera<sup>\*</sup>, Leonardo Caprio, Barbara Previtali, Ali Gökhan Demir

Department of Mechanical Engineering, Politecnico di Milano, Via La Masa 1, 20156 Milan, Italy



## ARTICLE INFO

## Keywords:

Beam shaping  
Irradiance profile  
Ring beams  
Beam modeling  
Laser powder bed fusion  
Additive manufacturing

## ABSTRACT

Active fibre lasers are widely used in the industry for different manufacturing applications ranging from cutting, to welding and additive manufacturing. The recent introduction of the multiple-core fibre lasers allows these sources to flexibly change the Power Density Distribution (PDD) from conventional Gaussian profiles towards ring shapes. While the advantages of the novel beam shapes over the conventional ones are still being explored, the need for modeling tools to define the PDD shapes becomes more evident. This work studies the analytical modeling of Gaussian to ring profiles with the aim to move towards standardized parameters referable to the manufacturing processes. The proposed models combine Gaussian and annular components to define the novel beam shapes. Among the different models assessed, the Torus and Multi-Gaussian approaches exhibited the best fitting quality thus enabling the definition of descriptive metrics of the PDD. The modeling framework developed was validated on an industrial Laser Powder Bed Fusion (LPBF) system with a double-core light source. The beam shape variation along the propagation axis was assessed to analyze the effect of defocusing using the developed beam parameters. Eventually, the best performing model was furtherly validated with a bead on plate experiment to explain how the model coefficients can be jointly exploited to predict the material response using a Gaussian or a ring beam profile.

## 1. Introduction

High-power fibre lasers have emerged as the established standard sources in many industrial manufacturing processes ranging from welding, cutting, and additive manufacturing [1–4]. These lasers operate in Continuous (CW) or Pulsed Wave (PW) regimes of power modulation, delivering beams that are focused on the workpiece to achieve proper spot sizes depending on the application. Despite significant advancements in laser performance over the years, including power levels, stability, wavelength range, and temporal versatility, the flexibility of laser beam shape has remained limited [5,6]. In LPBF technology, as well as in laser welding and cutting applications that require higher power levels, Gaussian beam distributions have traditionally been regarded as the standard [2,7]. However, numerous studies in the literature have cast doubt upon the suitability of the Gaussian distribution for material

processing. Indeed, this power density distribution is often believed to cause large thermal gradients [8–10], undue overheating [9,11–14], defects [9,10,14,15], and suboptimal material processing performance [5,6,9,10,14,16,17]. To address these challenges, spatial beam shaping has been proposed as a solution to tailor the energy input and manipulate the induced thermal field.

Beam shaping includes all those techniques aimed at the manipulation of the light characteristics. Among the most addressed metrics in industrial applications, the Power Density Distribution (PDD) emerges as the most important. Also referred as irradiance or spatial beam profile, this property defines the power distribution in a plane orthogonal to the light propagation axis. Other customizable beam characteristics are the temporal profile of power, addressed as temporal beam shaping, and the wavelength of the beam, which is usually modified to optimize the power absorption of reflective materials [18–21].

*Abbreviations:* I, irradiance, MW/cm<sup>2</sup>;  $\hat{I}$ , relative irradiance, %;  $I_{pk}$ , peak intensity, MW/cm<sup>2</sup>;  $I_r$ , ring intensity, MW/cm<sup>2</sup>; r, radial position,  $\mu\text{m}$ ;  $\Delta r$ , beam profiler resolution,  $\mu\text{m}$ ;  $\Delta z$ , focus position, mm;  $w_G$ , Gaussian radius,  $\mu\text{m}$ ;  $w_1$ , ring radius,  $\mu\text{m}$ ;  $w_{G2}$ , ring half width,  $\mu\text{m}$ ;  $w_D$ , doughnut radius,  $\mu\text{m}$ ; BSi, beam shape index, non-dimensional;  $\theta$ , beam divergence, mrad; P, laser power, W; v, scan speed, mm/s;  $w_m$ , melt pool width,  $\mu\text{m}$ ;  $h_t$ , melt pool depth,  $\mu\text{m}$ ; AR, melt pool aspect ratio, non-dimensional;  $\alpha$ , power partition, %; K, irradiance scale factor, MW/cm<sup>2</sup>; L, localisation, non-dimensional;  $w_{86}$ , beam radius (86 % power cutoff),  $\mu\text{m}$ .

<sup>\*</sup> Corresponding author.

*E-mail addresses:* [francesco.galbusera@polimi.it](mailto:francesco.galbusera@polimi.it) (F. Galbusera), [leonardo.caprio@polimi.it](mailto:leonardo.caprio@polimi.it) (L. Caprio), [barbara.previtali@polimi.it](mailto:barbara.previtali@polimi.it) (B. Previtali), [aligokhan.demir@polimi.it](mailto:aligokhan.demir@polimi.it) (A.G. Demir).

<https://doi.org/10.1016/j.jmpro.2024.02.069>

Received 19 October 2023; Received in revised form 2 February 2024; Accepted 28 February 2024

Available online 22 March 2024

1526-6125/© 2024 The Authors. Published by Elsevier Ltd on behalf of The Society of Manufacturing Engineers. This is an open access article under the CC BY-NC-ND license (<http://creativecommons.org/licenses/by-nc-nd/4.0/>).

Regarding laser-based processes featuring high power levels, such as welding, cutting or LPBF, two spatial beam shaping approaches have emerged from the literature, defined as static and dynamic in-source beam shaping [22,23]. This distinction is solely based on the laser beam perspective in its path along the optical architecture. It is important to underline that the adopted terminology for the two approaches must be referred as a categorical distinction of the numerous technologies attempted in the literature and not as a rule to distinguish among the actual working principle of the spatial beam shaping technologies.

The static approach involves the use of a beam shaper lens within the optical chain to modify the standard Gaussian shape provided by commercially available single mode laser sources. Typically, the beam shaper is a refractive or diffractive based optic positioned within the optical chain, between the collimator and the focusing lens. The laser beam is first collimated through achromatic lenses, then a beam shaper lens imparts the desired PDD and eventually the resulting beam is focused onto the working plane [8,12,14,17,24–27]. Certain lenses, such as  $\pi$ -Shapers [17], exhibit PDD characteristics that vary with the working distance from the focusing lens. Consequently, the desired beam shape may not be readily available at the focal plane of the lens. In some cases, high-quality beam shaper lenses provide a combination of collimation and power redistribution, eliminating the need for a dedicated collimator after the fibre end [14]. Regardless of the lens specifications, the static approach generally requires modifications to the existing optical chain of industrial machines or in-house architectures. Although this feature may entail additional system complexity and cost as well as limited compatibility with automated production [5], static optical elements can guarantee the maximum freedom in terms of spatial transformation as each lens is designed for a bespoke PDD.

Conversely, the in-source dynamic approach does not require the introduction of new hardware in the optical chain but relies on special technologies capable of engineering the beam directly within the laser source and flexibly during the process. Some technologies employ special perturbation mechanisms or envelopes multiple independent fibre laser source to partition the power in a multi-core assembly of the feeding fibre. Others exploit the diffraction patterns generated by the coherent overlapping of multiple phased and independent single mode beams. Some of these novel laser sources are now available for laser welding, cutting, and LPBF applications [5,28,29].

The use of beam shaping techniques has already proved many benefits in high-power laser applications. Specifically, enhanced cutting quality and productivity have been demonstrated when using multi-core fibre lasers for O<sub>2</sub> and N<sub>2</sub> laser cutting of mild steel and stainless steel, respectively [5]. Multi-core laser sources allowed to improve the stabilization of the keyhole channel and to reduce the spattering when welding mild steels [6] or wrought aluminum alloys [30]. A similar technology was employed to tailor the weld microstructure to prevent hot cracking of AA6005 [31] or to control the microstructure and the intermetallic compound of the weld seam in a multi-material joint application made of steel and aluminum [32]. Other novel laser sources manipulated the irradiance profile of the laser beam by acting on the multiple interference of laser beams, demonstrating an enlargement of the welding feasibility window of AA3003 [33]. Laser beam oscillation has also been explored as an alternative dynamic beam shaping strategy in laser cutting [34] and laser welding [35] to manipulate the power distribution felt by the material, although this technique is commonly applied with Gaussian beams. With regards to the LPBF process, static beam shaping approaches allowed to increase the process robustness, i. e. tailoring a bespoke PDD to counteract the occurrence of defects (like cracks or pores) [8,12,16,24–26,36–41]. Recent studies have demonstrated the application of innovative PDDs, specifically ring profiles generated by multi-core fibre laser sources, in LPBF processes involving materials such as AISI316L [42–44], AlSi7Mg0.6 [45], AA5083 [46], Scalmalloy [47] Ti6Al4V [48] and Fe2.9Si [49].

Regardless of the approach, the scientific literature has demonstrated how spatial beam shaping solutions can enhance the process flexibility

while keeping a moderate-to-high adaptation level to already existing systems. Nonetheless, the diverse working principle of these technologies can significantly complicate the interpretation of results and the already challenging physics lying behind laser-matter interaction. Therefore, to dictate new guidelines to establish beam shaping as a reproducible tool, the experimental effort cannot exclude the analytical modeling of the laser beams and the introduction of new mathematical tools capable of providing a precise description of the tool. As a matter of fact, customized PDDs cannot be simply synthesized using beam diameter and total power, as commonly done for standard Gaussian distributions. Instead, more descriptive parameters that consider the actual shape of the beam must be quantitatively characterized for non-Gaussian PDDs.

From the literature various beam modeling efforts have emerged, including Gaussian beams [26,50–55], Bessel beams [37,56], annular beams such as pure doughnut or toroidal profiles [12,26,56–60], and flat-top-like beams [12,26,52,61]. Recently, there have been attempts to reconstruct ring beams by employing a superposition of a Gaussian and an annular component [62,63]. These modeling efforts aim to provide insights into the characteristics and behaviour of different beam profiles, facilitating their accurate representation and utilization in laser processes.

Therefore, in this study, three analytical models were developed under the hypothesis that ring beams can be synthesized by combining a Gaussian and an annular beam. First, the models were tested by reproducing the shape of the available PDD in their focal plane based on optical acquisition datasets of the beams. For a representative ring beam, the effectiveness of the ring model was assessed also along the propagation axis. Then, the most effective model was validated through a bead-on-plate experiment, which tested the Gaussian and a representative ring beam. The experiment involved the variation of power, scan speed, and focus position, to thoroughly assess the performance and reliability of the selected model.

## 2. Modeling of the power density distribution

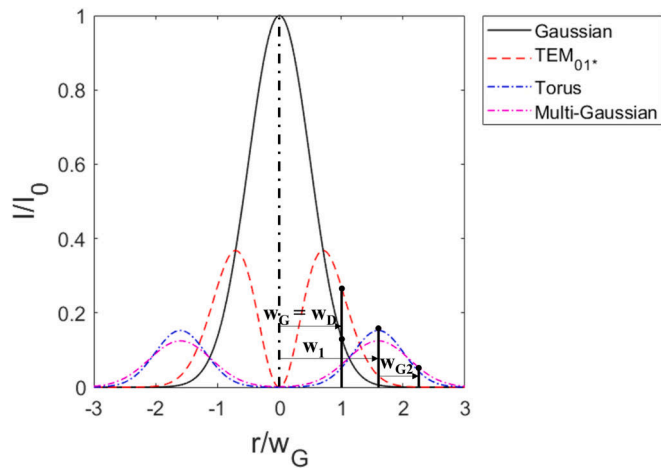
This section provides a mathematical description of the Gaussian and various annular beam models, namely the Torus, Multi-Gaussian, and pure doughnut models. These analytical models are derived from the Laguerre-Gaussian modes, which serve as the standard for classifying Transverse Electromagnetic Modes (TEM) [64]. According to the definition, these modes are solutions to Maxwell's equations featuring a radially symmetric intensity distribution [65]. Their structure can be synthesized with the subscripts  $p$  and  $l$  (TEM <sub>$p$</sub> ), which identify the number of radial and angular zero fields, respectively [66–68]. Additionally, this section introduces superimposed models that combine a Gaussian and an annular component. These models have been proposed to effectively represent the ring profiles generated by the novel laser source utilized in this study.

Fig. 1 illustrates a comparison of the main PDDs used to design the ring beams and the basic nomenclature. Shapes are normalized to the same power and the Gaussian beam radius ( $w_G$ ). For annular beams, the position of the annular intensity peaks is identified with  $w_1$ , whereas half of the ring width with  $w_G$ . In Fig. 1, the radius of the pure doughnut beam (TEM<sub>01+</sub>), denoted with  $w_D$ , has the same radius of the Gaussian beam radius.

For any PDD the localisation can be calculated using the formula mentioned in Eq. (1) [50].

$$L = \frac{3\langle r^4 \rangle}{2\langle r^2 \rangle^2} \quad (1)$$

where  $\langle r^2 \rangle$  and  $\langle r^4 \rangle$  are the second and the fourth moments of the PDD, respectively, and can be calculated as follows:



**Fig. 1.** PDDs of different shapes normalized to the same power and the Gaussian beam radius ( $w_G$ ).  $w_1$  indicates the position of the annular intensity peaks whereas  $w_{G2}$  denotes half the ring width. The doughnut beam radius is identified with  $w_D$ .

$$\langle r^2 \rangle = \frac{2\pi}{P} \int_0^{R_{max}} r dr r^2 I(r) \tag{2}$$

$$\langle r^4 \rangle = \frac{2\pi}{P} \int_0^{R_{max}} r dr r^4 I(r)$$

The upper integration limit,  $R_{max}$ , is restricted to  $R_{max} \approx 3 \sqrt{2 \langle r^2 \rangle}$  according to the ISO 11146. The parameter  $L$  represents a dimensionless shape-encoding parameter that quantitatively describes how power is localised within the PDD. For any rotationally symmetric PDD, it can be mathematically demonstrated that  $L \geq 3/2$ . In the case of a pure Gaussian PDD,  $L$  is equal to 3. The second and the fourth order moments consist in a sum of contributions which depend on the local intensity  $I(r)$  of the PDD and are weighted by the radial coordinate at the second and fourth power, respectively. Since the fourth power  $r^4$  attributes higher weights to the annular region of a PDD, localisation value can increase or decrease depending on the structure of the PDD. Consistently, the laser power is said to be well or poorly localised within the beam radius when the PDD decreases rapidly or slowly with the radial coordinate, respectively.

In the literature, localisation has been employed to decode the structure of non-Gaussian beams by differentiating the equivalent power fractions in the core or the annular region of a PDD [50]. In this work, superimposed analytical models were proposed to decode the structure of ring beams. Hence,  $L$  was just calculated to provide a benchmark of power localisation for the various tested beam shapes.

**2.1. Gaussian model**

The radial intensity distribution of a Gaussian beam ( $I_G$ ) can be expressed with the following model [69]:

$$I_G(r) = \frac{2P_G}{\pi w_G^2} e^{-2\left(\frac{r}{w_G}\right)^2} \tag{3}$$

where  $P_G$  is the laser power,  $w_G$  denotes the beam radius defined according to UNI ISO11146 ( $1/e^2$  cut off). This mode structure corresponds to the  $TEM_{00}$ , which stands out as the most common TEM for the laser sources due to the minimal diffraction losses within the resonating cavity [64,69].

Eq. (3) demonstrates that a Gaussian laser beam can be fully described with two parameters: the total power and the beam radius. When the beam radius remains constant, an increase in laser power leads to a higher peak intensity at the center of the PDD. Conversely, under the

same laser power, larger beam radii result in a reduction of the peak intensity. Fig. 2a–b illustrates the effects of power ( $P_G = 150\text{--}250$  W,  $w_G = 25$   $\mu\text{m}$ ) and radius ( $w_G = 25\text{--}45$   $\mu\text{m}$ ,  $P_G = 200$  W) on the intensity profile, respectively.

**2.2. Annular models**

**2.2.1. Torus**

The Torus intensity model ( $I_T$ ) can be represented by the following expression [57]:

$$I_T(r) = \frac{\frac{3P_T}{w_{G2}^2} e^{-\frac{3(r-w_1)^2}{w_{G2}^2}}}{\pi \left( e^{-3\left(\frac{w_1}{w_{G2}}\right)^2} + \sqrt{3\pi} \frac{w_1}{w_{G2}} \left( 1 + \text{erf}\left(\sqrt{3} \frac{w_1}{w_{G2}}\right) \right) \right)} \tag{4}$$

In this model,  $P_T$  is the total laser power,  $w_{G2}$  is half of the torus width and  $w_1$  is the ring radius identifying the annular peak intensity. The Torus PDD is derived from the assumption of a three-dimensional Gaussian intensity distribution with a toroidal shape and centered at the origin. Details of the analytical calculations can be found in the work of Zapata et al. [57].

Eq. (4) demonstrates that the toroidal PDD is fully described by three beam parameters: the total power ( $P_T$ ), the half the torus width ( $w_{G2}$ ) and the ring radius ( $w_1$ ). Fig. 3a–c illustrates the effects of power ( $P_G = 150\text{--}250$  W,  $w_{G2} = 25$   $\mu\text{m}$ ,  $w_1 = 50$   $\mu\text{m}$ ), half the torus width ( $w_{G2} = 25\text{--}45$   $\mu\text{m}$ ,  $P_T = 200$  W,  $w_1 = 50$   $\mu\text{m}$ ) and ring radius ( $w_1 = 50\text{--}100$   $\mu\text{m}$ ,  $P_T = 200$  W,  $w_{G2} = 25$   $\mu\text{m}$ ) on the intensity profile, respectively. When the half torus width and ring radius remain constant, a power increase leads to higher annular intensity peaks. Conversely, under the same ring radius and power, larger half torus widths result in a decrease of the

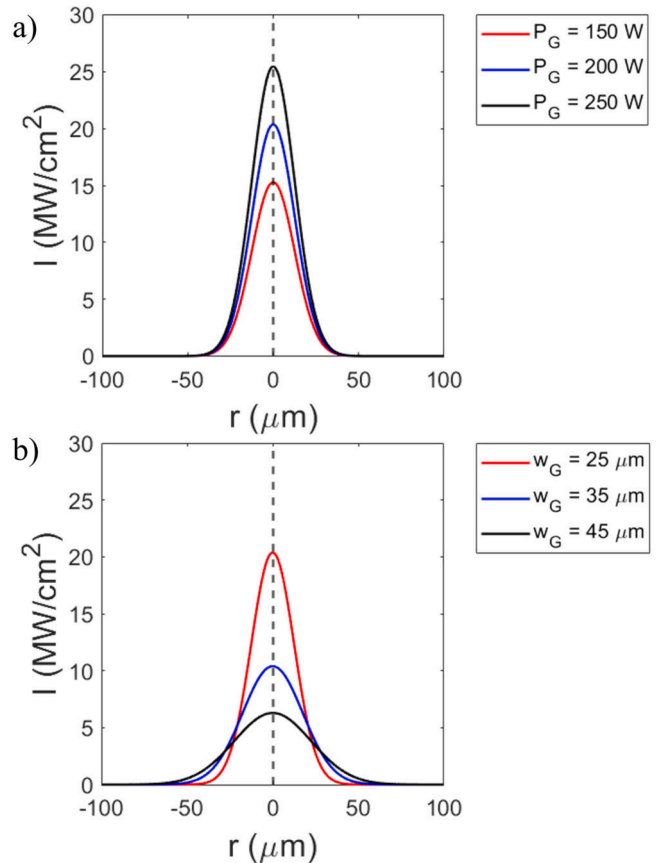


**Fig. 2.** Effect of Gaussian beam parameters. a) Effect of  $P_G$  (with  $w_G = 25$   $\mu\text{m}$ ); b) effect of  $w_G$  (with  $P_G = 200$  W).

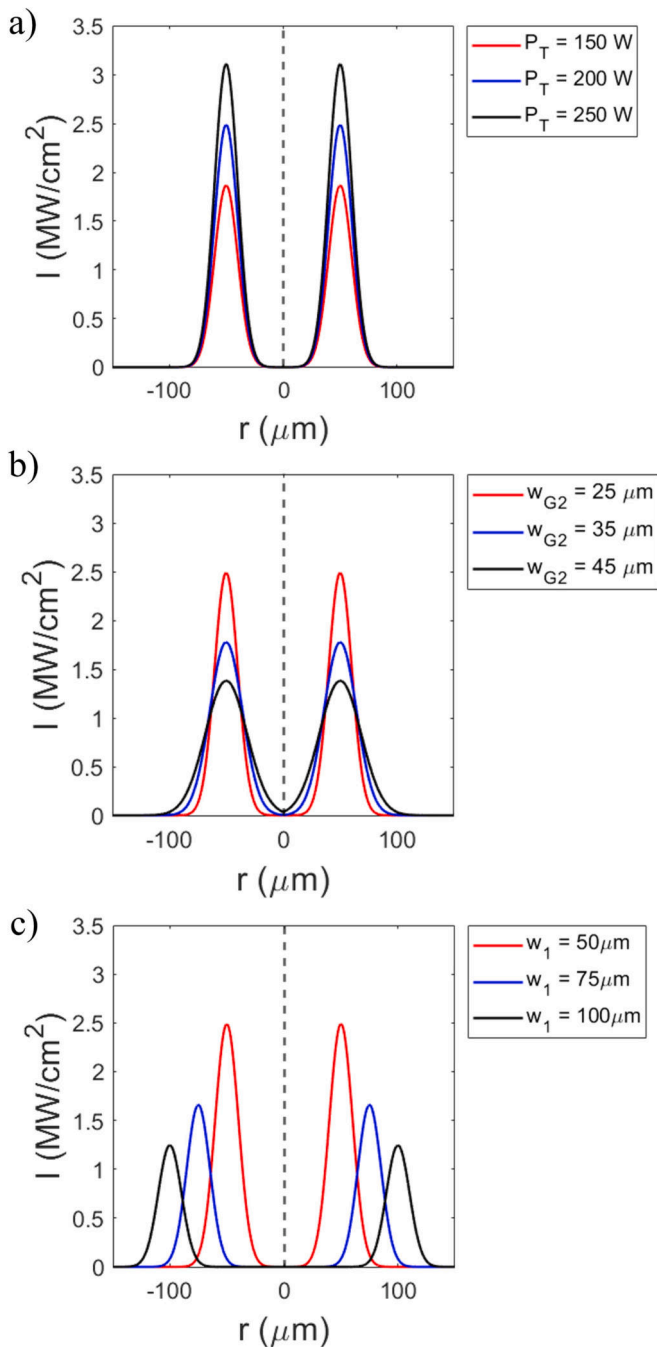


**Fig. 3.** Effect of Torus beam parameters. a) Effect of  $P_T$  (with  $w_{G2} = 25 \mu\text{m}$  and  $w_1 = 50 \mu\text{m}$ ); b) effect of  $w_{G2}$  (with  $P_T = 200 \text{ W}$ ,  $w_1 = 50 \mu\text{m}$ ); c) effect of  $w_1$  (with  $P_T = 200 \text{ W}$ ,  $w_{G2} = 25 \mu\text{m}$ ).

annular intensity peak.

Using the Laguerre-Gaussian terminology, the Torus model closely resembles the  $TEM_{01}^*$  definition when the ring radius significantly exceeds the half torus width. Under this condition, the PDD is entirely annular, and the intensity at the origin is negligible. However, as depicted in Fig. 3b, when the half torus width approaches the ring radius, a discontinuity point emerges at the origin, where the intensity is expected to be zero for a pure  $TEM_{01}^*$  mode.

The sole effect of the ring radius is twofold: it causes the annular peaks to shift away from the origin, and their intensity decreases with larger ring radii. Although the intensity reduction may appear counterintuitive, Eq. (4) represents a closed analytical form where the conservation of total laser power must hold true, regardless of the half torus

width and ring radius. Therefore, the reduction in annular intensity is compensated by the additional intensity content concentrated in the central part of the PDD within the toroidal peaks.

### 2.2.2. Multi-Gaussian

The Multi-Gaussian model is defined as the sum of two identical Gaussian PDDs, which are positively and negatively shifted in the radial domain. The analytical model can be defined as follows [56,57]:

$$I_{MG,2D}(r) = \frac{2P_{MG}}{\pi w_{G2}^2} \left( e^{-2\left(\frac{r-w_1}{w_{G2}}\right)^2} + e^{-2\left(\frac{r+w_1}{w_{G2}}\right)^2} \right) \quad (5)$$

In this mode,  $P_{MG}$  and  $w_{G2}$  are the total laser power and the beam radius of each independent Gaussian component, whereas  $w_1$  is the radial shift, or ring radius, which determines the position of the Gaussian peaks. Note that Eq. (5) defines an open model where the conservation of total laser power is not necessarily achieved. However, by properly integrating the model and constraining the total laser power, it can be reduced to a toroidal PDD.

The Multi-Gaussian approach offers more flexibility and accuracy when fitting annular PDDs compared to a Torus model. This is because the annular intensity peak is independent of the ring radius. Therefore, three independent beam parameters are employed to describe the Multi-Gaussian model: the laser power ( $P_{MG}$ ) and beam radius ( $w_{G2}$ ) for each Gaussian component and the ring radius or radial shift ( $w_1$ ). Fig. 4a–c illustrates the effects of power ( $P_{MG} = 150\text{--}250 \text{ W}$ ,  $w_{G2} = 25 \mu\text{m}$ ,  $w_1 = 50 \mu\text{m}$ ) and radius ( $w_{G2} = 25\text{--}45 \mu\text{m}$ ,  $P_{MG} = 200 \text{ W}$ ,  $w_1 = 50 \mu\text{m}$ ) of each independent Gaussian component, and ring radius ( $w_1 = 50\text{--}100 \mu\text{m}$ ,  $P_{MG} = 200 \text{ W}$ ,  $w_{G2} = 25 \mu\text{m}$ ) on the intensity profile.

The impact of the laser power and beam radius of each independent Gaussian component is similar to that discussed for the Torus intensity profile. However, a key difference is illustrated in Fig. 4c, where higher ring radii cause the Gaussian components to shift away without affecting their intensities.

### 2.2.3. $TEM_{01}^*$

The  $TEM_{01}^*$ , or pure doughnut, consists of the superposition of two orthogonal  $TEM_{01}$  modes, namely the  $TEM_{01}$  and the  $TEM_{10}$ . The resulting distribution represents an annular beam with a central zero [12,26,64]. The analytical model can be derived from the generic Laguerre-Gaussian mode and expressed as follows [12,26]:

$$I_{TEM_{01}^*}(r) = \frac{2P_{TEM}}{\pi w_D^2} \frac{2r^2}{w_D} e^{-2\left(\frac{r}{w_D}\right)^2} \quad (6)$$

where  $P_{TEM}$  is the laser power and  $w_D$  is a characteristic beam radius of the doughnut.

Unlike the Torus and Multi-Gaussian models, the position of the annular peaks in a  $TEM_{01}^*$  ( $w_1$ ) is not independent of the doughnut radius ( $w_D$ ). In fact, it can be mathematically demonstrated that the ring radius identifying the position of the annular peaks is  $w_1 = \pm\sqrt{2} w_D/2$ .

Therefore, a  $TEM_{01}^*$  mode can be fully described using two beam parameters: the total power ( $P_{TEM}$ ) and the doughnut radius ( $w_D$ ). When the doughnut radius remains constant, an increase in laser power leads to a higher peak intensity at the center of the PDD. Conversely, under the same laser power, the intensity of the annular peak decreases with larger doughnut radii. Fig. 5a–b illustrates the effects of power ( $P_{TEM} = 150\text{--}250 \text{ W}$ ,  $w_D = 25 \mu\text{m}$ ) and radius ( $w_D = 25\text{--}45 \mu\text{m}$ ,  $P_{TEM} = 200 \text{ W}$ ) on the intensity profile, respectively.

### 2.3. Superimposed beam models

In the literature, a specific type of PDD called “ring profiles” has been introduced, which features the superposition of a Gaussian component located at the center and an annular component [5,42–45,70].

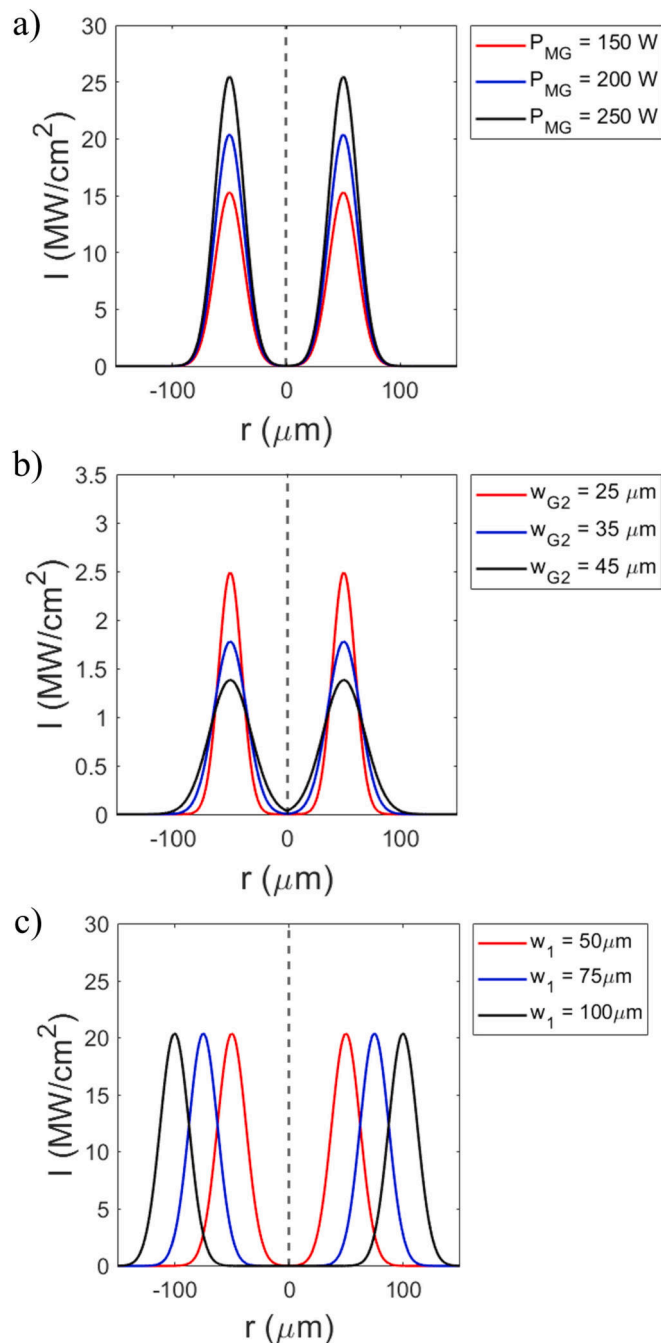


**Fig. 4.** Effect of Multi-Gaussian beam parameters. a) Effect of  $P_{MG}$  (with  $w_{G2} = 25 \mu\text{m}$  and  $w_1 = 50 \mu\text{m}$ ); b) effect of  $w_{G2}$  (with  $P_{MG} = 200 \text{ W}$ ,  $w_1 = 50 \mu\text{m}$ ); c) effect of  $w_1$  (with  $P_{MG} = 200 \text{ W}$ ,  $w_{G2} = 25 \mu\text{m}$ ).

Although, the term ring is more suited to denote pure annular beams like doughnuts, the nomenclature “ring beams” or “ring-shaped profiles” has now gained significant attention, particularly in high-power laser welding, cutting and LPBF applications, due to the development of novel laser sources that utilize multi-core feeding fibres. The mathematical representation of ring beams involves designing a combined model that includes a central Gaussian component with an annular PDD. Depending on the approach used to model the annular component, three analytical forms of ring beams have been proposed: the Torus (T + G), the Multi-Gaussian (MG + G), and the  $TEM_{01}^*$  ( $TEM_{01}^* + G$ ). Table 1 resumes the mathematical formulas of the proposed ring beams ( $I_R$ ). Differently from the proposed analytical formulations, the superimposed models shown in Table 1 feature some variations, namely a coefficient of power

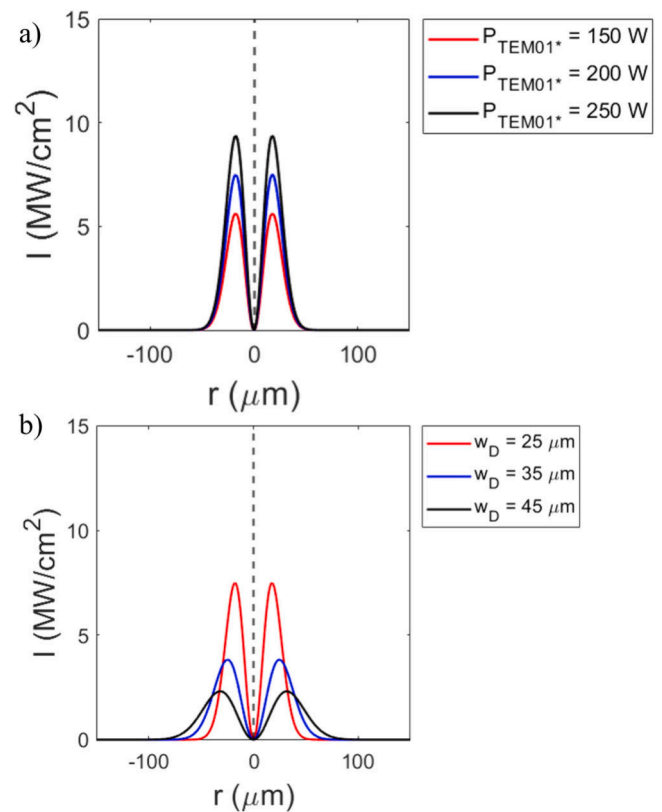


**Fig. 5.** Effect of  $TEM_{01}^*$  beam parameters. a) Effect of  $P_{TEM}$  (with  $w_D = 25 \mu\text{m}$ ); b) effect of  $w_D$  (with  $P_{TEM} = 200 \text{ W}$ ).

partition ( $\alpha$ ) and the total power encompassed by the beam profile ( $P_{tot}$ ), which were introduced for the nonlinear regression fitting using the models based on Torus and  $TEM_{01}^*$  definitions. The complete procedure for the nonlinear regression is explained in Section 3.

The modeling of ring PDDs using a superposition of Gaussian and annular profiles is driven by the design principles of novel multi-core fibre laser sources with beam shaping capabilities. These sources employ power partitioning within the guiding regions of the feeding fibre, combining the central core responsible for generating a Gaussian profile with the surrounding ring responsible for generating an annular intensity. The resulting ring shape is predominantly influenced by the beam component with higher power. However, it is important to note that the power partition within the feeding fibre does not necessarily align with the power fractions of the Gaussian and annular components used to define the shape of the ring PDD.

### 3. Methodology

#### 3.1. Beam source and optical configurations

To demonstrate the applicability of the various proposed models, optical acquisitions and experiments were conducted using a novel double-core fibre laser source (Corona nLIGHT AFX 1000, nLIGHT Inc., Vancouver, Washington, USA). This technology exploits an in-source mechanism within the feeding fibre to partition the power between its inner core and the surrounded annular region [5]. The working principle allows to operate with a Gaussian PDD, when the laser power is concentrated in the core, or with unconventional ring PDDs, when power is split between the core and the annular guiding region of the fibre. The user cannot control freely the power partition as the source is designed to operate with seven pre-defined power settings, each of which identifies a different beam profile. For sake of simplicity, the index BSi was assigned for each power setting, with i ranging from 0 to

**Table 1**

Definition of superimposed models with their analytical formulas and coefficients to be estimated via nonlinear regression.

Ring models	Symbol	Analytical formulas	Coefficients to be estimated
Torus + Gaussian	T + G	$I_R(r) = \frac{3P_{tot}(1-\alpha)}{\pi w_{G2}^2} e^{-3\frac{(r-w_1)^2}{w_{G2}^2} + \frac{2P_{tot}\alpha}{\pi w_G^2} e^{-2\left(\frac{r}{w_G}\right)^2}}$ $\pi \left( e^{-3\left(\frac{w_1}{w_{G2}}\right)^2} + \sqrt{3\pi} \frac{w_1}{w_{G2}} \left( 1 + \operatorname{erf}\left(\sqrt{3} \frac{w_1}{w_{G2}}\right) \right) \right)$	$\alpha, w_G, w_1, w_{G2}$
Multi-Gaussian + Gaussian	MG + G	$I_R(r) = \frac{2P_{MG}}{\pi w_{G2}^2} \left( e^{-2\left(\frac{r-w_1}{w_{G2}}\right)^2} + e^{-2\left(\frac{r+w_1}{w_{G2}}\right)^2} \right) + \frac{2P_G}{\pi w_G^2} e^{-2\left(\frac{r}{w_G}\right)^2}$	$P_{MG}, P_G, w_G, w_1, w_{G2}$
TEM <sub>01*</sub> + Gaussian	TEM <sub>01*</sub> + G	$I_R(r) = \frac{2P_{tot}(1-\alpha)}{\pi w_D^2} \frac{2r^2}{w_D^2} e^{-2\left(\frac{r}{w_D}\right)^2} + \frac{2P_{tot}\alpha}{\pi w_G^2} e^{-2\left(\frac{r}{w_G}\right)^2}$	$\alpha, w_G, w_D$

6. Table 2 shows the nominal power settings in terms of power fraction between the guiding regions of the fibre declared by the producer.

As illustrated in Table 2, a rising BS index corresponds to a growing power fraction delivered in the annular core of the feeding fibre. The power fraction of the index BS0 corresponds to a Gaussian PDD. Instead, indices BS1-6 identify ring PDDs, being featured by a central peak of power surrounded by a ring of annular intensity.

The employed laser source could emit either in Continuous Wave (CW) or Pulsed Wave (CW) regimes of power modulation, operating with a maximum power of 600 W for the index BS0 up to 1.2 kW for the index BS6. This source was integrated into an existing industrial LPBF architecture (3D-NT LLA150, Torino, Italy). Two optical architectures were utilized throughout this study. One was dedicated to the beam measurements and reconstruction (“optical configuration 1”) whereas the other, which consists of an industrial architecture for high-power applications (up to 1 kW), was used for beam measurements and bead on plate experimentation (“optical configuration 2”). A schematization of the optical architectures is depicted in Fig. 6a–b.

For the optical configuration 1 (shown in Fig. 6a), the architecture comprised beam collimation (OPI Photonics, Torino, Italy), light conveyance through two reflective mirrors, beam manipulation (Raylase MS-III, Raylase, Weßling, Germany) and focusing (Ronar, Qioptiq, Waltham, US) onto the workplane. A beam expander unit was also positioned in the light path, after collimation and before the scanning head, as illustrated in Fig. 6a. This arrangement allowed to increase the size of the collimated beam diameter before focalization, facilitating the generation of adequate focal spots ideal for intricate and thin part features for LPBF applications. For the optical configuration 2 (Fig. 6b), the beam was focused and manipulated with a different scanning head (AM Module, Raylase, Weßling, Germany) which comprised a focusing system made of two lenses, one of which is motorized, rather than an F-Theta lens. In this configuration, the focalization of the laser beam is obtained by setting the absolute vertical coordinate of the motorized lens, whose micro adjustments are electronically coordinated and synchronized with galvo scanners by a control unit anytime the beam is deflected. This configuration also features the same collimation setup of the first configuration and a dichroic mirror which enables the integration of additional on-axis monitoring setup [71,72], which was not used in this experimental activity.

In summary, the optical configuration 1 consists in the standard setup integrated in the LPBF system. This optical configuration allows to operate with power levels lower than 200 W, which is the power threshold of the f-Theta lens to prevent severe focus shift effects. The

**Table 2**

Nominal power fraction declared by the producer for each beam shape.

Beam shape, BSi	BS0	BS1	BS2	BS3	BS4	BS5	BS6
Power fraction % (core/ring)	100/0	70/30	60/40	50/50	40/60	20/80	10/90

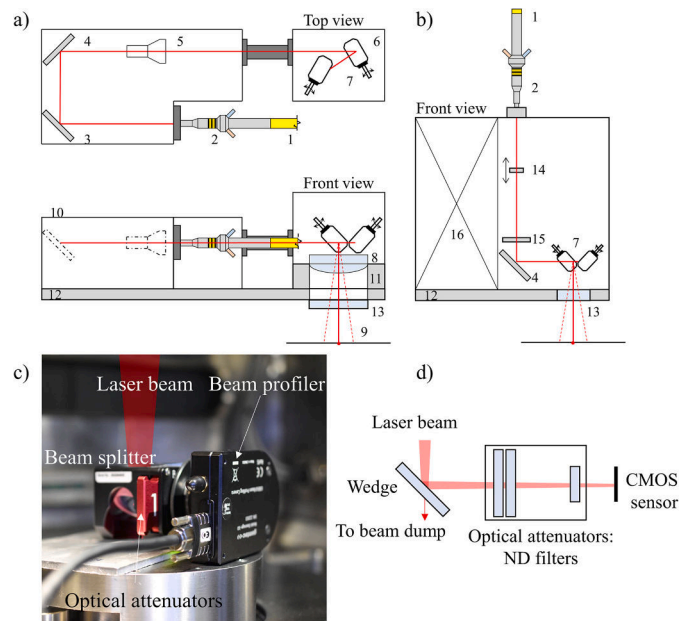


**Fig. 6.** a–b) Optical configurations 1 (beam sampling) and 2 (bead on plate): 1 - feeding fibre, 2 - collimating unit, 3 - reflective mirror, 4 - dichroic mirror, 5 - beam expander unit, 6 - scanning head, 7 - galvo scanners, 8 - F-theta lens, 9 - scanning area, 10 - sealed box for optics, 11 - scanning head support, 12 - optical bench, 13 - protective glass, 14 - motorized focusing lens, 15 - fixed focusing lens, 16 - on-axis monitoring module. c) Optical setup employed for the beam measurements; d) Schematization of light propagation within the optical setup.

integration and employment of the optical configuration 2 is motivated by the need to conduct experimental tests at power levels above 200 W.

### 3.2. Beam imaging and power measurement

Optical acquisitions were conducted along the light propagation axis using a beam profiler (Gentec Beamage Series USB 3.0, Quebec City, Canada) in the optical configuration 1 (see Fig. 6a). The camera employed a CMOS sensor with dimensions of 11.3 × 11.3 mm<sup>2</sup>, a spatial resolution of 5.5 μm/pixel, and a declared maximum power density on the sensor of 10 W/cm<sup>2</sup> with an ND4.0 filter. To safeguard the sensor

from potential damage, the beam profiler was coupled with a beam splitter and multiple optical attenuators (ND filters). The beam splitter consisted of two orthogonally oriented wedges that reflected <0.0001 % of the beam to the CMOS sensor and prevent the formation of ghost images on it, while the remaining part of the incident laser beam was directed towards a beam dump. The optical setup used for sampling the beams and a schematic depicting light propagation are illustrated in Fig. 6c–d. Optical acquisitions were performed following the standard UNI EN ISO11146 with similar optical setup used in the literature [46,73–76].

Each available PDD (indices BS0-6) was reconstructed in the focal plane at a fixed average power of 200 W (CW) and characterized prior to beam sampling using a power meter (W-3000-D55-SHC, Laserpoint, Vimodrone, Italy). Multiple acquisitions along the light propagation axis were performed in the vicinity of the focal plane only for index BS4, with a Δz = 0.5 mm spacing between the acquisition points. These additional measurements constituted an ideal case study plan aimed at evaluating the influence of tolerance in beam positioning on the actual PDD shape.

With the same beam imaging setup, additional beam measurements were performed using the optical configuration 2 (see Fig. 6b) at the same average power of 200 W but only for the indices BS0 and BS4, which were exploited to validate the models thought bead on plate experiments.

The beam profiler software (Beamage v1.07) allowed to export spatially resolved data in terms of relative intensity (Î). The relative intensity data (%) were converted into dimensional intensity (MW/cm<sup>2</sup>) by considering that the integral of the PDD in space (r, θ) corresponds to the total average power utilized in the test (200 W). Given the reasonable assumption that the PDD exhibits a rotational symmetry property, the PDD does not depend on θ. Therefore, by introducing an appropriate scaling factor K for irradiance (% to MW/cm<sup>2</sup>) and considering that the beam data are discretized in space, the total power encompassed by the PDD can be calculated using the following summation:

$$P = \sum_{i=-R_{max}}^{i=R_{max}} \pi * I_i * |r_i| * \Delta r = \sum_{i=-R_{max}}^{i=R_{max}} \pi * K * \hat{I}_i * |r_i| * \Delta r \quad (7)$$

Here, Δr represents the sensor resolution whereas r<sub>i</sub> denotes the radial position of each acquisition point. Consequently, by knowing the total laser power of the test, K can be calculated using the following equation:

$$K = \frac{P}{\pi \Delta r \sum_{i=-R_{max}}^{i=R_{max}} \hat{I}_i * |r_i|} \quad (8)$$

The integration is performed on a subset of the measured data to prevent background noise from dominating the integrals, as defined by the standard UNI EN ISO11146. R<sub>max</sub> is determined as R<sub>max</sub> ≈ 3 √(2<r<sup>2</sup>><sup>2</sup>), where <r<sup>2</sup>><sup>2</sup> represents the second order moment of the PDD [50].

In the analysis of the raw dataset, the beam radius w<sub>86</sub> was estimated for each PDD using the convention of 86 % of total power enclosed. These results were compared to the estimations obtained from the beam profiler, which applies the standard 1/e<sup>2</sup> cutoff. It is important to note that the 1/e<sup>2</sup> cutoff is coincident with the 86 % power inclusion only for a pure Gaussian beam. Beam divergence (θ) is a measure of the beam diameter enlargement with increasing distance along the beam propagation axis. It was calculated according to the experimental procedures defined by the standard UNI EN ISO11146.

### 3.3. Nonlinear regression

The ring models, as listed in Table 1, were employed to perform nonlinear regression analysis on the two-dimensional acquisitions of the PDDs using Matlab (MathWorks, Natick, Massachusetts, USA). A Matlab function based on a sum of squares minimization algorithm was utilized

to estimate the model coefficients. To ensure the validity of the estimated values, additional positivity constraints were imposed on each coefficient to prevent the generation of physically implausible estimations, such as negative radii.

For each PDD, the primary coefficients of interest are the Gaussian component radius, w<sub>G</sub>, and the annular component radii, namely w<sub>1</sub> and w<sub>G2</sub> for the Torus and Multi-Gaussian models, and w<sub>D</sub> for the TEM<sub>01\*</sub> model. Additionally, for the models involving the Torus and TEM<sub>01\*</sub> components, the power partition coefficient α is fitted. This coefficient determines the percentage of the total test power (P<sub>tot</sub>) allocated within either the Gaussian or annular component. However, in the case of the Multi-Gaussian model, the definition of α is not feasible due to Eq. (5), which defines an open analytical model where P<sub>MG</sub> represents the power of each shifted Gaussian component, rather than the total power encompassed by the PDD. Consequently, for the Multi-Gaussian approach, the power values P<sub>G</sub> and P<sub>MG</sub>, in addition to the radii w<sub>G</sub>, w<sub>1</sub>, and w<sub>G2</sub>, are fitted, and α is calculated based on the fitted power values (i.e. P<sub>G</sub>/P<sub>tot</sub>). After determining the model coefficients, the Multi-Gaussian approach was assessed by verifying the total power encompassed by the curve, which should align with the test power value of 200 W.

To facilitate the fitting of the ring PDD, a straightforward approach involves setting α for the Torus and TEM<sub>01\*</sub> models, or P<sub>G</sub> and P<sub>MG</sub> for the Multi-Gaussian model, according to the nominal power fractions specified in Table 2 for the multi-core feeding fibre. However, it is crucial to note that the declared power fraction within the guiding regions of the feeding fibre may deviate from the actual power fractions (Gaussian and annular) in the vicinity of the focal plane.

Regarding the validity range of the applied ring models, it is important to assess the condition w<sub>1</sub> > w<sub>G2</sub> for the approaches incorporating the Torus and the Multi-Gaussian, as depicted in Fig. 7a. This condition prevents the algorithm from fitting an annular component that closely resembles a Gaussian component. Outside of this range, the annular peaks tend to shift closer to the origin, causing the PDD to approach a TEM<sub>00</sub> shape. This scenario typically arises when fitting Gaussian-like PDDs or ring PDDs far from the focus position, where the simple Gaussian model of Eq. (3) provides a better fit compared to the ring model.

However, when considering the ring model based on the pure TEM<sub>01\*</sub> definition, the same condition cannot be applied. This is due to the interdependence of the ring radius, w<sub>1</sub>, and doughnut radius, w<sub>D</sub>, as well as the presence of a zero-intensity point at the origin within the TEM<sub>01\*</sub> model. In such cases, a heuristic approach can be employed to prevent the algorithm from overfitting a ring model when a simple Gaussian model is sufficient. As illustrated in Fig. 7a, this approach involves verifying that the fitted TEM<sub>01\*</sub> component of the ring model remains fully enclosed within the fitted Gaussian component, and also ensuring that w<sub>D</sub> ≤ w<sub>G</sub>, where w<sub>D</sub> and w<sub>G</sub> are the fitted doughnut and gaussian radii.

It is important to emphasize that these conditions are imposed solely to improve the fitting quality for Gaussian-like PDDs or ring-like PDDs far from the focus position. They are not based on physical assumptions but rather serve as guidelines to ensure accurate fitting results.

### 3.4. Model validation through bead-on-plate experiments

An experimental plan was designed to validate the analytical modeling of the beam profiles with a practical example of focus position variation. For sake of simplicity, only one representative ring beam profile was chosen, namely index BS4, and its effect compared with the Gaussian profile, that is index BS0. Multiple bead on plate were realized with optical configuration 2 (Fig. 6b) to test two power levels (200–400 W) in a large spectrum of scan speeds (100–1000 mm/s with step of 225 mm/s). To investigate the effect of focus position on the PDD, three different positions along the propagation axis were chosen. Specifically, the focus position of each index (Δz = 0 mm) and two symmetrical

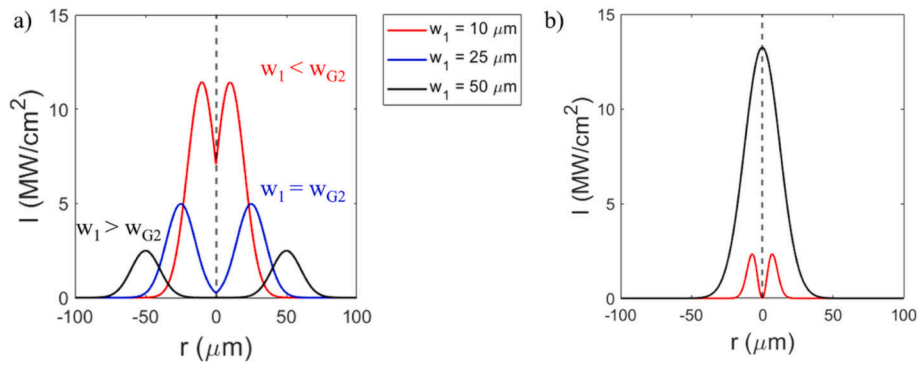


Fig. 7. a) Validity condition for Torus/Multi-Gaussian models based on  $w_1$  and  $w_{G2}$ ; b) Validity condition for  $TEM_{01^*}$  model based on  $w_D$ ,  $w_G$  and power enclosed in  $TEM_{01^*}$  shape.

Table 3

Fixed and varied process parameters used in the bead on plate experiment.

Fixed parameters	
Inert gas type	Argon
Baseplate material	AISI304
Baseplate thickness (mm)	5
Varied parameters	
Beam shape, BS (-)	BS0, BS4
Power, P (W)	200, 400
Scan speed, v (mm/s)	100, 325, 550, 775, 1000
Focus position, $\Delta z$ (mm)	-1.5, 0, 1.5

positions before and after the focus ( $\Delta z = \pm 1.5$  mm) were tested. Fixed and varied process parameters of the bead on plate experiment are listed in Table 3.

The experiment was conducted on AISI304 stainless steel plate. The tracks were then cut with an automatic linear saw without any deformation and prepared with conventional metallographic procedures, as shown in Fig. 8a. Melt pool boundaries were revealed with an etchant made of HNO<sub>3</sub>, HCl and H<sub>2</sub>O (even volumetric concentrations). Melt pool dimensions in terms of width ( $w_t$ ), depth ( $h_t$ ) and aspect ratio ( $AR = h_t/w_t$ ) were collected for each experimental condition, as depicted in Fig. 8b. For each track two measurements of the melt pool dimensions were collected.

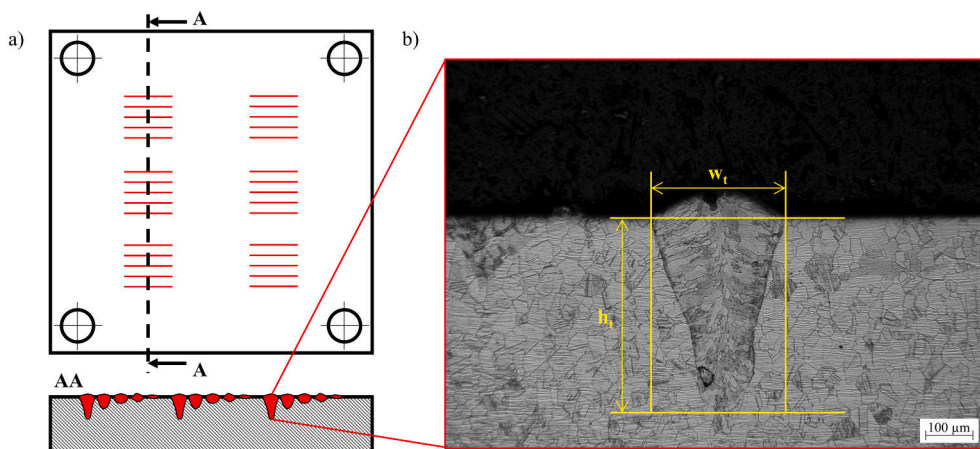


Fig. 8. a) Schematization of bead on plate experiment on a stainless plate with detail of the melt pools; b) melt pool dimensions in terms of width  $w_t$  and depth  $h_t$ .

## 4. Results

### 4.1. Model fitting with superimposed models at focal position

After acquiring the beams in their focal position using optical configuration 1 (see Fig. 6a), each of the proposed model was tested to fit the optical datasets. Fig. 9 depicts the optical acquisitions and the fitted irradiance profiles for each beam shape (BS) and tested model.

For index BS0, each fitted ring model exhibited an annular component that was fully enclosed within the dominant Gaussian. However, the conditions  $w_1 > w_{G2}$  for the ring models incorporating the Torus (T + G) and Multi-Gaussian components (MG + G), and  $w_D > w_G$  for the ring model based on the  $TEM_{01^*}$  definition ( $TEM_{01^*} + G$ ), were not satisfied. This implicitly demonstrates that the utilization of ring models to fit a pure  $TEM_{00}$  beam may not be appropriate. Fig. 9 also illustrates the fitting of index BS0 using a simple Gaussian model (G), as presented in Eq. (3), with  $\alpha$  (rather than  $P_G$ ) and  $w_G$  as the parameters to be fitted. Overall, the Gaussian model allowed to achieve the same intensity profile fitted by ring models, although the number of coefficients to be estimated, and thus the complexity of the model, was significantly reduced.

For the other indices BS1-6, the ring models accurately fitted the data, indicating that ring beams require more shape-encoding parameters than those of Gaussian beam to be fully described. Indeed, at least in their focal plane, the conditions  $w_1 > w_{G2}$  for the T + G and MG + G models, and  $w_D > w_G$ , for the  $TEM_{01^*} + G$  model, were always satisfied. As the BS index increases, which means a rising power fraction in the ring of the feeding fibre, the fitted annular components gradually dominated the shape of the PDD.

Table 4 presents the adjusted  $R^2$  ( $R_{adj}^2$ ) values of the attempted

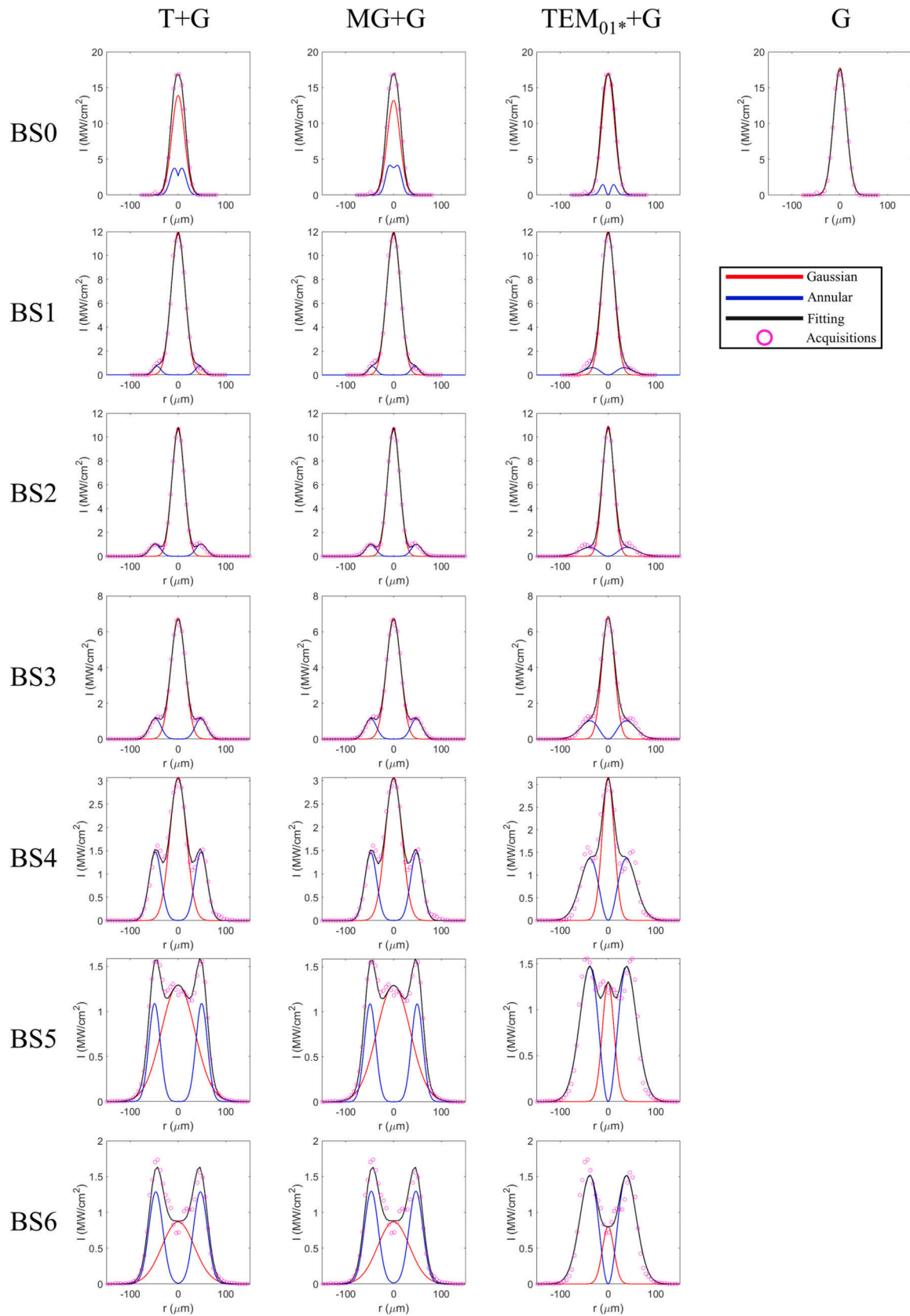


**Fig. 9.** Fitted ring PDD along with the Gaussian and the annular components of each beam shape (BS) and each ring model. For index BS0 the fitting with a Gaussian model is also shown. Note the different scale bar for the various tested beam shapes. G stands for Gaussian, T for Torus, MG for Multi-Gaussian. Note that the irradiance axis is scaled differently for each beam shape for better readability. Results belong to optical configuration 1.

**Table 4**  
Adjusted  $R^2$  ( $R_{adj}^2$ ) values for the attempted beam models. G stands for Gaussian, T for Torus, MG for Multi-Gaussian.

BS (-)	$R_{adj}^2$			
	G	T + G	MG + G	TEM <sub>01*</sub> + G
BS0	99.58	99.80	99.79	99.81
BS1	–	99.63	99.61	99.52
BS2	–	99.89	99.89	99.66
BS3	–	99.79	99.79	99.40
BS4	–	99.13	99.15	97.50
BS5	–	99.58	99.58	96.98
BS6	–	98.25	98.22	95.93

models for each tested BS. Concerning the index BS0, the  $R_{adj}^2$  of the Gaussian model (G) was slightly lower compared to the results obtained with ring models, but the model complexity was reduced significantly, as only two parameters are fitted. For all the other indices BS1-6, the highest fitting quality could be achieved with T + G and MG + G models, as their  $R_{adj}^2$  kept always above 98 %. Conversely, the TEM<sub>01\*</sub> + G model was always outperformed. This could be attributed to the mathematical definition of TEM<sub>01\*</sub>, which featured a zero intensity in the origin and an interdependence between the radial peaks position ( $w_1$ ) and the doughnut radius ( $w_D$ ). As depicted in Fig. 9, this limitation appeared clearly for indices BS2-6, where the fitting of the annular intensity peaks was less accurate.

For the MG + G model and each index, the total power enclosed by the profile was calculated and compared with the test power (200 W) as the power defined in the model (see Eq. (5)) represents only the power of each Gaussian component incorporated in the model. As only few discrepancies in the range of few W were observed, which could be attributed to background noise of the optical acquisition, the fitting with

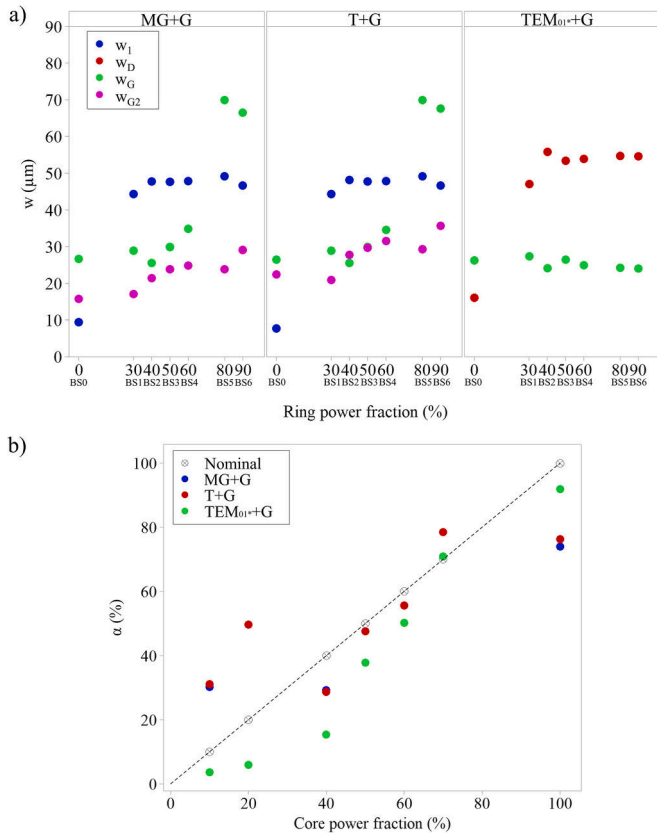
this model was considered valid.

Fig. 10a illustrates the fitted coefficients in terms of beam radii for each BS and ring model. When modeling ring profiles based on Torus or Multi-Gaussian definitions, the profiles indexed with BS1-6 exhibit a stable ring radius ( $w_1$ ) ranging from 44 to 49  $\mu\text{m}$  and an increasing half torus width ( $w_{G2}$ ) ranging from 20  $\mu\text{m}$  to 30  $\mu\text{m}$  with a rising BS index. Despite the similarities between the two annular models, it is important to note that the Torus model tends to overestimate the radii  $w_{G2}$  compared to the Multi-Gaussian model for the same BS index. This difference arises from the definitions of  $w_{G2}$  for the two models, where the Multi-Gaussian approach considers 86 % of the power enclosed, while the Torus approach considers 95 % of the power, as demonstrated by Zapata et al. [57]. A similar trend was observed when modeling with the TEM<sub>01\*</sub> mode (pure doughnut), where the fitted diameter  $w_D$  stabilized at 49–55  $\mu\text{m}$ . The beam radius of the fitted Gaussian components  $w_G$  also exhibited similarities between the Torus and Multi-Gaussian approaches. For BS1-4,  $w_G$  remained between 25 and 29  $\mu\text{m}$ , but significantly increased to 67–69  $\mu\text{m}$  for BS5-6. On the other hand, the ring model based on the TEM<sub>01\*</sub> definition consistently fitted  $w_G$  between 24 and 27  $\mu\text{m}$  for any ring beam (indices BS1-6). The sudden increase in the fitted  $w_G$  for the Torus and Multi-Gaussian models could be attributed to the utilization of a larger Gaussian component to achieve a better fit in the central part of the ring profile, motivated by the weak positivity constraints imposed on the radii. Stronger constraints on the diameter would likely result in a more precise radius estimation while reducing the accuracy of the fitting.

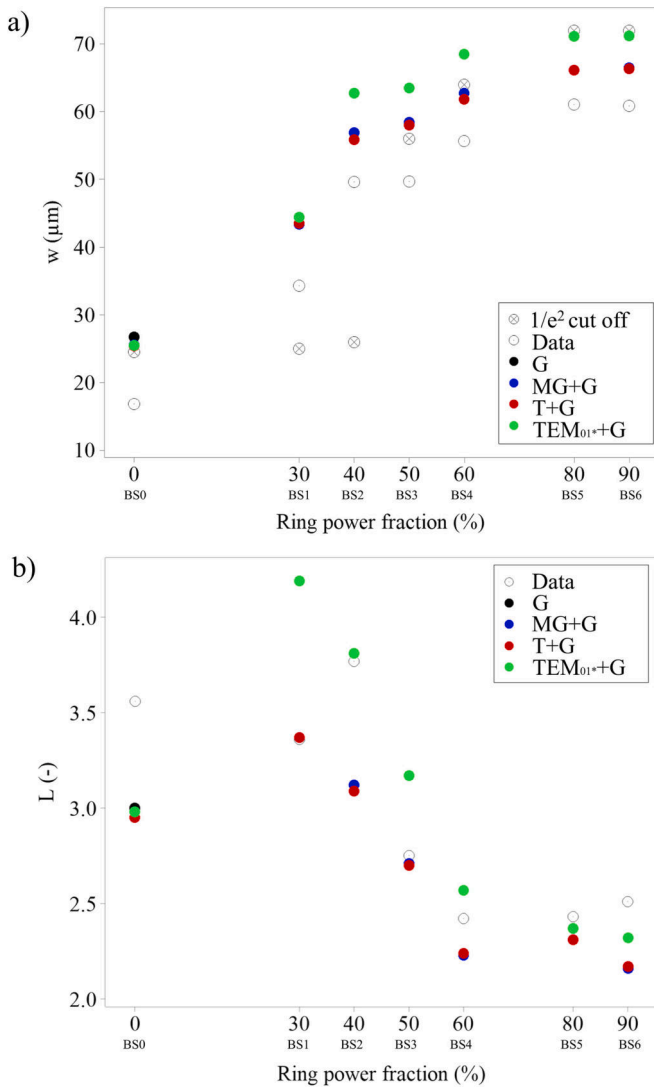
Fig. 10b shows the fitted coefficients in terms of Gaussian power fraction ( $\alpha$ ) as a function of the nominal core power fraction of the feeding fibre for each tested ring model. It is worth noting that for the ring model based on the Multi-Gaussian approach,  $\alpha$  was not fitted but calculated from the fitted model coefficients. Surprisingly, the TEM<sub>01\*</sub> approach could reproduce the trend of the nominal power partition within the feeding fibre, despite some discrepancies for indices BS4-5. In contrast, the Torus and Multi-Gaussian approaches only accurately reproduced the nominal power partition up to BS4, after which they started to deviate. However, as explained earlier in the context of the Gaussian component radius  $w_G$ , it is reasonable to assume that this deviation is a fitting inaccuracy of the algorithm influenced by the boundary conditions imposed on the model coefficients.

Fig. 11a depicts the beam radius  $w$  for the various ring power fractions tested. The radii were determined from the raw dataset using the cut off 86 % of total power enclosed (“Data” in the legend) and compared with the beam profiler radii based on the  $1/e^2$  convention. The same radii were also calculated from the fitted ring models using the 86 % cut off. The calculation of beam radii from the fitted PDD was motivated by the high fitting quality ( $R_{adj}^2$ ) achieved with these models, demonstrating their ability to accurately reproduce the PDDs regardless of the model coefficients. The same approach was used to calculate localisation, as shown in Fig. 11b, with the only difference being that the beam profiler data were not included as localisation could not be estimated by the software.

Overall, the estimations of  $w$  from the fitted models aligned with the radii calculated from the raw dataset and obtained from the beam profiler. The improved spatial discretization employed with the fitted PDDs helped to enhance the accuracy of the radius estimation compared to the raw data, which suffered from the low spatial resolution of the beam profiler sensor. For index BS0, the beam radius estimation derived from the raw dataset was consistently lower than the estimations based on the other fitted models (rings and Gaussian) and that obtained from the beam profiler based on the  $1/e^2$  cut off, which coincides with the 86 % of total power convention for a Gaussian beam. For indices BS1-2, the beam radius calculated with the beam remained nearly constant at 25–27  $\mu\text{m}$  and deviated from the estimations based on the 86 % cut off. In the case of Gaussian-like shapes, namely indices BS1-2, the estimation of this radius could be affected by uncertainty due to the dominant Gaussian component, which underestimated the effective value of the



**Fig. 10.** Model coefficients for each beam shape in the focal position in terms of a) radii and b) core power fraction. G stands for Gaussian, T for Torus, MG for Multi-Gaussian. Results belong to optical configuration 1.



**Fig. 11.** a) Beam radius ( $w$ ) and b) localisation ( $L$ ) for each beam shape (BS) and models. G stands for Gaussian, T for Torus, MG for Multi-Gaussian.  $1/e^2$  cut off and Beam Profiler refers to beam radius or localisation estimated from the beam profile software and the raw dataset, respectively. Results belong to optical configuration 1.

radius.

Regarding localisation, each of the fitted models correctly reproduced  $L$  for a Gaussian profile, which could be mathematically shown to be equal to 3. The  $L$  calculated from the raw data overestimated localisation, likely due to the limited amount of data caused by the poor spatial resolution of the beam profiler sensor. For all other indices BS1-6,  $L$  followed a decaying trend. Specifically, the ring beams BS1-2 exhibited an  $L$  value higher than the Gaussian one, indicating that for these PDDs the power was less localised within the beam radius compared to a Gaussian profile. Conversely, for all the other ring beams, the localisation value was lower than the Gaussian one, indicating that these for these PDDs the power featured a better localisation within the radius than a Gaussian profile. An exception should be made for the index BS3 modeled with  $TEM_{01*} + G$  for which the Gaussian shape exhibited a better localisation than the ring profile.

#### 4.2. Model fitting at different focal position

In this section, the focus is on investigating the variation of the PDD characteristics along the beam propagation axis for a specific beam

shape index, BS4. This index was chosen as a representative ring profile with an almost even nominal power allocation within the double-core fibre. Multiple beam measurements were taken at different positions along the light propagation axis. For this investigation, only the Torus approach (T + G) was used for the nonlinear regression fitting of the PDDs. This choice was based on the highest quality fitting observed among the proposed ring models, as demonstrated in the focal plane acquisitions for various indices, and the ease of defining the validity range of the Torus fitting. The goal was to understand the effects of potential errors in beam focusing on the actual shape of the PDD.

Fig. 12a shows the intensity distributions at various positions ( $\Delta z$ ) relative to the waist radius. As the position approached the F-theta lens ( $\Delta z > 0$  mm), the intensity profiles underwent significant changes, transitioning from a ring profile at the focal position ( $\Delta z = 0$  mm) to a Gaussian-like profile. The annular intensity peaks gradually decayed, and the overall shape degenerated into a Gaussian distribution. This is evident from the fitted ring profiles, where the annular component diminished rapidly, emphasizing the central Gaussian component. In Fig. 12b, at the boundary of the acquisition ( $\Delta z = 1.5$  mm), the ring radius ( $w_1$ ) became smaller than half torus width ( $w_{G2}$ ), rendering the use of a ring profile inefficient for the fitting. This observation was consistent with the coefficient of power allocation ( $\alpha$ ) shown in Fig. 12c, which rapidly increased up to 100% when a pure Gaussian model was used for fitting. Notably, at  $\Delta z = 1.0$  mm, which represented a transitional condition, the ring radius was prone to deviate. Despite the validity condition of the ring model ( $w_1 > w_{G2}$ ) was still satisfied, there was a sudden increase in the mean value from 46 to 48  $\mu\text{m}$  to 59  $\mu\text{m}$ .

On the other hand, as the position moved away from the F-theta lens ( $\Delta z < 0$  mm), the variation in PDD shape was more restrained, although there was a general reduction in intensity due to a larger beam size. The fitted coefficients  $w_1$  and  $\alpha$  followed a stable trend, while  $w_{G2}$  was expected to increase and eventually degenerate ( $>w_1$ ) as the proper distance from the waist was reached. However, this degeneration was not yet observed at the other acquisition boundary ( $\Delta z = -1.5$  mm), indicating that the fitting with a ring model was still valid. The asymmetry of the intensity distribution before and after the focal plane is likely due to the presence of the F-Theta lens. For such lens, the paraxial approximation may not be valid and the beam propagation before and after the focal plane can differ.

Fig. 12d presents the beam radii ( $w_{86}$ ) at each acquisition point. The calculation of  $w_{86}$  was performed on the raw dataset, although there might be a moderate underestimation of their real values due to the spatial resolution of the beam profiler (as seen in Fig. 11a). The data revealed the typical caustic propagation trend of Gaussian beams along their propagation axis and beam radius passed from 55  $\mu\text{m}$  in the focal position to around 65–70  $\mu\text{m}$  at 1.5 mm far from it.

#### 4.3. Effect of focus position on the melt pool geometry

In this section, the effect of focus position on the melt pool characteristics is presented through the results of the bead on plate experiment. This experiment was carried out with optical configuration 2 (see Fig. 6b) and was supported by multiple beam measurements at various focus positions at a fixed average power of 200 W.

Fig. 13 displays the metallographic cross sections obtained at a fixed power level (200 W) and scan speed (100 mm/s), with the corresponding irradiance profiles at each various focus positions, for the two tested beam profiles, namely BS0 and BS4.

Fig. 14a–c presents the melt pool geometry characteristics, namely depth ( $h_p$ ), width ( $w_p$ ) and aspect ratio (AR), as a function of scan speed, for each beam profile and combination of laser power and focus position.

The melt pool geometry characteristics exhibited an inverse relationship with scan speed, irrespective of power level, focus position, and beam profile. These results aligned with existing welding literature, as the linear energy density decreases with increasing speed [64]. The

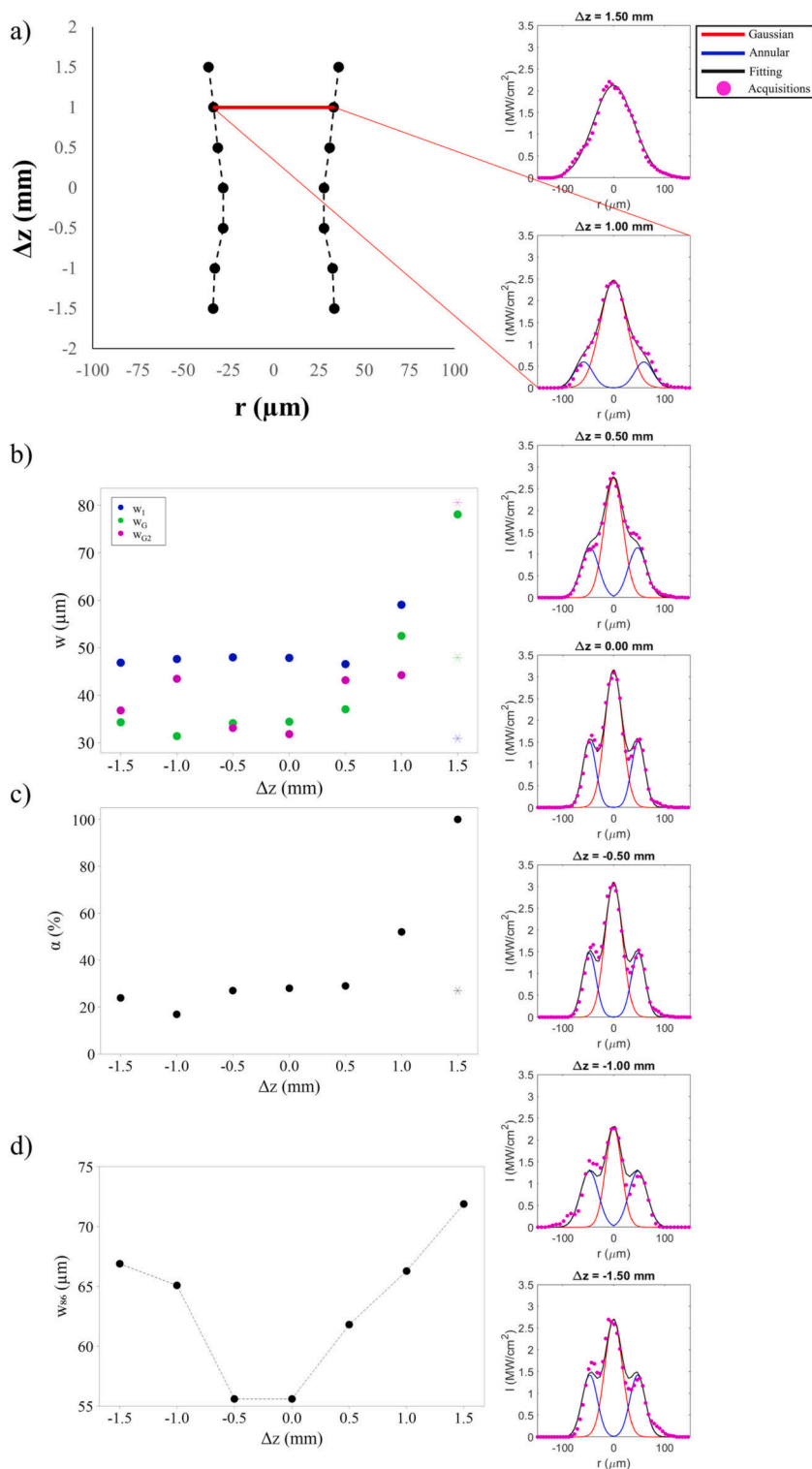


**Fig. 12.** a) Beam propagation and intensity distributions ( $I$ ) at various relative distances ( $\Delta z$ ) for index BS4. Model coefficients in terms of b) radii and c) power fraction and d) beam radius ( $w_{86}$ ) for each  $\Delta z$  position.  $\Delta z$  denotes the relative distance from the waist radius. Positive  $\Delta z$  approaches the F-theta lens. Ticked crosses indicate the coefficients fitted with ring profile outside its validity range  $w_1 < w_{G2}$  which are replaced with a pure Gaussian model. Results belong to optical configuration 1.

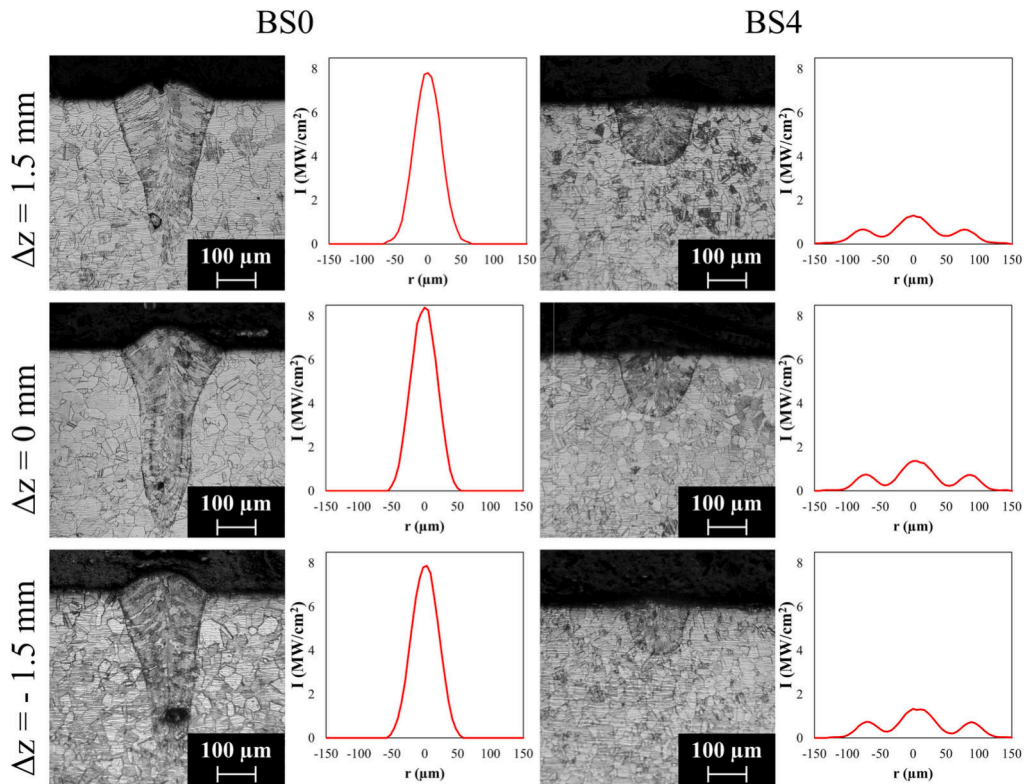


Fig. 13. Metallographic cross sections of the beads on plate obtained at various focus position ( $\Delta z$ ) at a power and scan speed level of 200 W and 100 mm/s, respectively, for the two tested beam profiles BS0-4. For each condition, the measured irradiance profiles in terms of  $I$  ( $\text{MW}/\text{cm}^2$ ) and radial coordinate  $r$  ( $\mu\text{m}$ ) are shown. Results belong to optical configuration 2.

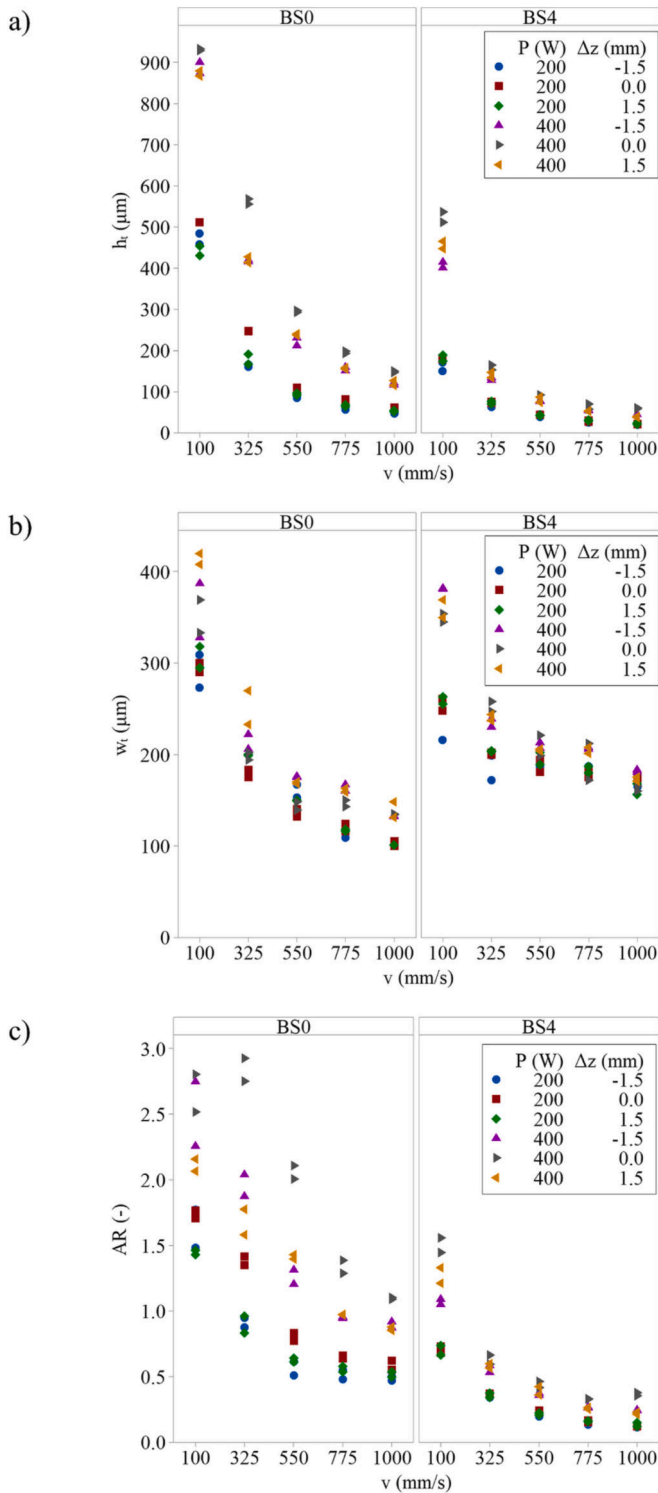
effect of focus position was evident in the melt pool depth graph depicted in Fig. 14a. Indeed, for a given power and regardless of the beam profile, higher penetration depths were observed when working in the focal position due to a higher intensity peak and a smaller beam spot. While the effect on melt pool width was challenging to discern as, theoretically, in the focal plane of the beam, smaller melt pool width is expected, the same trend observed for  $h_t$  held also for the melt pool aspect ratio. Main trends and effects of varied process parameters were validated through analysis of variance, as reported in Fig. 1a–b and Table 1 of the Supplementary material. Fig. 14a–b clearly demonstrated the effect of ring profile (index BS4) in comparison with the Gaussian distribution (index BS0). With the same power level and focus position, the melt pool depth obtained under the ring profile was consistently lower than that achieved with a Gaussian distribution, irrespective of the scan speed. Conversely, the melt pool width decreased less rapidly for the index BS4, attaining at 160–180  $\mu\text{m}$  at  $v = 1000 \text{ mm/s}$  depending mostly on the power level. This effect was expected and could be attributed to the larger spot size of the index BS4 than the Gaussian one (209  $\mu\text{m}$  vs 77  $\mu\text{m}$  with  $1/e^2$  cut off in the focal position) and to the smaller beam radius variation as well as changes in the intensity distribution within the investigated depth of field ( $\Delta z = \pm 1.5 \text{ mm}$ ), as shown in Fig. 13.

Fig. 14c also demonstrated the occurrence of the keyhole mechanism and its transition to conduction melting mechanism with scan speed. Considering a melt pool AR of 0.8 as threshold for keyhole trigger [77], the Gaussian mode achieved deep penetration mode for a larger scan speed spectrum (up to 1000 mm/s with  $P = 400 \text{ W}$  and up to 550 mm/s with  $P = 200 \text{ W}$  in the focal position) than the ring profile. This result was attributable to the beam profile itself, whose power localisation leads to higher intensity peaks towards the center of the PDD. On the contrary, the ring profile exhibited deep penetration only at the minimum speed and maximum tested power ( $v = 100 \text{ mm/s}$  and  $P = 400 \text{ W}$ ), although the minimum intensity for keyhole initiation with steels,

namely  $1 \text{ MW}/\text{cm}^2$ , was guaranteed even at 200 W, regardless of the focus position (see the peaks in Fig. 13). This behaviour may be attributable to a more even power density distribution within the beam spot. An example of the melt pool geometry and the occurrence of these melting mechanisms under different beam profiles (BS0 vs BS4) could be observed with Fig. 13. The selected AR threshold for conduction to keyhole melting came from a recent work dealing with the same substrate material used throughout this research [77], although other smaller values (such as 0.4) are sometimes used in LPBF [78]. The correct melting transition should be identified with other in-situ monitoring techniques such as X ray imaging [79–81] or high-speed imaging [71,72], but are far beyond the scope of this work.

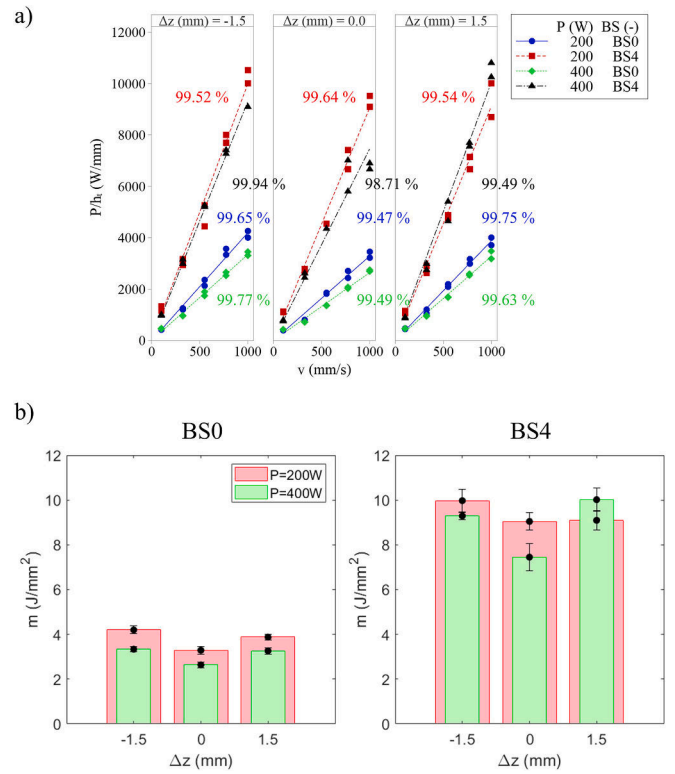
Fig. 15a shows the power over penetration depth ratio  $P/h_t$  as a function of the scan speed, for each focus position and combination of power and beam profile.  $P/h_t$  combines an input parameter, laser power, with an output measurement, melt pool depth, to define the overall penetration efficiency. This parameter is typically employed in the laser cutting process (considering the thickness of the metal sheet rather than  $h_t$ ), or in welding (considering the weld pool depth) [64]. It could be observed that this ratio followed a linear growing trend with scan speed, regardless of the focus position and power-beam shape combination [64]. Linear regression fits with corresponding adjusted  $R^2$  were reported in the graph. As appeared, for a given focus position, scan speed and power level, the difference in  $P/h_t$  between the two profiles (BS0 vs BS4) defined an efficiency gain intrinsic to the PDD when absolute penetration depth was the primary concern. In other words, the ratio suggested the total power gain that should be encompassed within two beam profiles to guarantee the same penetration depth. In these terms, index BS0 was more efficient than index BS4 since it consistently outperformed the ring profile irrespective of the varied parameters.

Fig. 15b displays the angular coefficients ( $m$ ) of each linear regression fits shown in the  $P/h_t$  vs  $v$  graph. The slope of the fits, dimensionally consisting of input energy per unit area ( $\text{J}/\text{mm}^2$ ), implicitly



**Fig. 14.** Melt pool depth ( $h_t$ ), width ( $w_t$ ) and aspect ratio (AR) as a function of the scan speed ( $v$ ) for the tested power levels (P), focus positions ( $\Delta z$ ) and beam profiles (BS). Results belong to optical configuration 2.

demonstrated the effect of the focus position for each beam profile. Indeed, as indicated from the barplot, this energy was always lower in the focus position ( $\Delta z = 0$  mm) than outside the focal plane. As expected, this implies that, at least in terms of penetration depth, working in the focal plane of the beam was more efficient, irrespective of the beam profile.



**Fig. 15.** a) Power over penetration depth ( $P/h_t$ ) as a function of the scan speed for various focus positions, laser power (P) and beam profiles (BS). Regression lines and corresponding  $R_{adj}^2$  are displayed to reveal linear trends for each combination of laser power and beam profile. b) Average and 95 % confidence intervals of the fitted angular coefficient ( $m$ ) of the linear regression trends ( $P/h_t$  vs  $v$ ). Results belong to optical configuration 2.

## 5. Discussion

The study revealed that the complex ring beams from the double-core fibre laser could be accurately described using new parameters. Two models, T + G and MG + G, were found to be the most effective, outperforming others in reproducing ring beam structures. Notably, the  $\text{TEM}_{01^*} + \text{G}$  model faced limitations due to dependencies in its geometric radii. The investigation extended beyond the focal plane, validating the chosen models. However, at the boundary of acquisition, a significant shape transformation occurred in the analyzed PDD, rendering the superimposed model ineffective, while the adoption of a simple Gaussian model provided a more robust fit.

In the subsequent part of this study, the proposed analytical models were validated with a bead on plate experiment. Specifically, the experiment was designed to elucidate how the interplay between beam profile and focus position influences melt pool morphology. To achieve this objective, optical configuration 2 was utilized along with two beam profiles, namely Gaussian (index BS0) and ring (index BS4). Fig. 16a displays the caustic beam propagation of the two tested beam profiles and the intensity distributions at the various focal positions. The raw intensity dataset is plotted alongside the fitted annular and Gaussian components of the ring model. For simplicity, only the T + G model was utilized for the ring profile. The results unequivocally demonstrated that the optical configuration 2 was less sensitive to variations in focus position than optical configuration 1, as both the beam radii ( $w_{86}$ , with 86 % of power cut off) and the intensity distributions did not undergo significant changes. Although the estimated beam divergence ( $\theta$ ) of index BS4 is almost twice than the index BS0, namely 24.78 mrad against 13.69 mrad, in the vicinity of the focal plane the ring beam

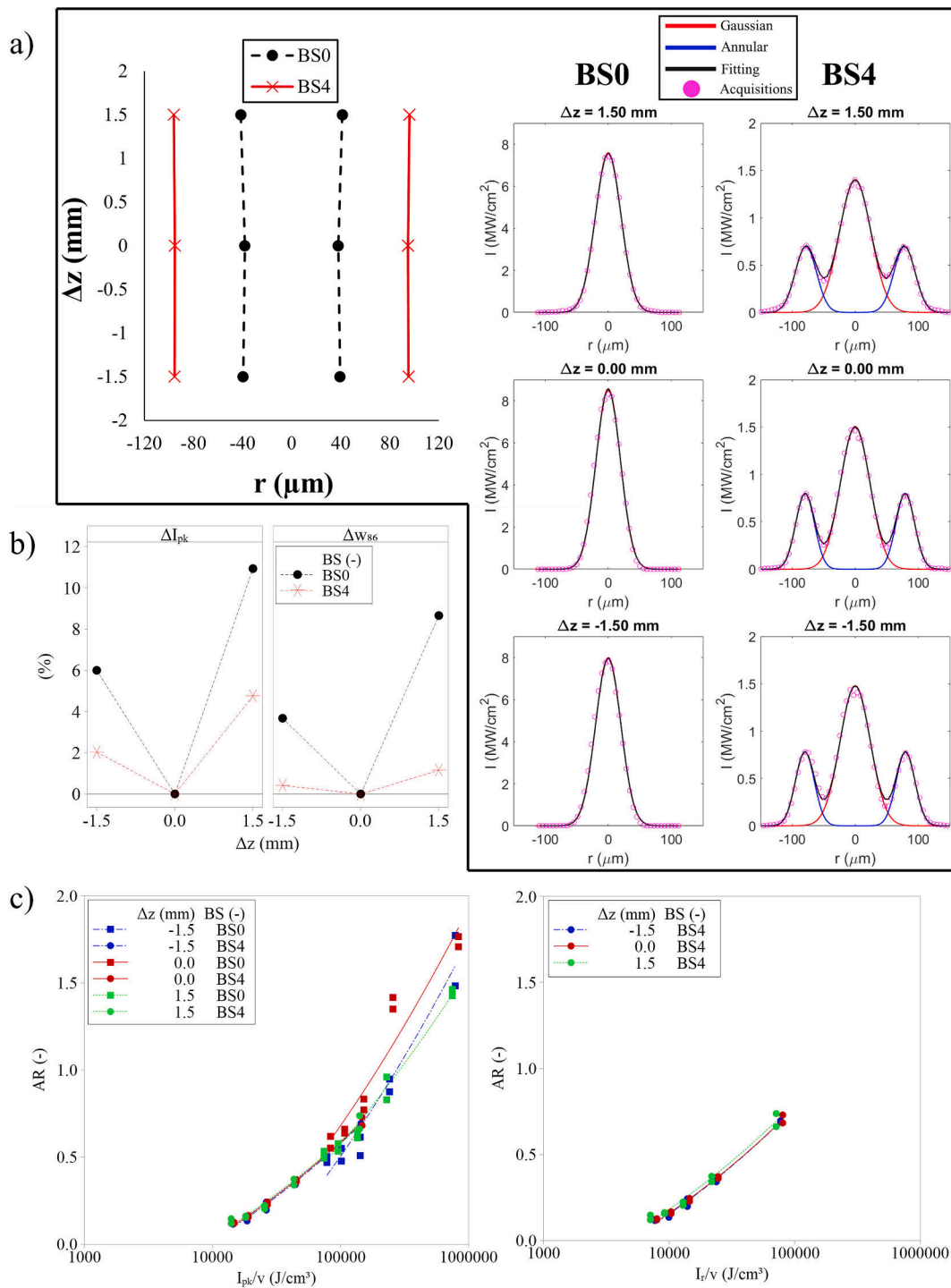


**Fig. 16.** a) Beam propagation and intensity distributions ( $I$ ) at various focal positions ( $\Delta z$ ) for indices BS0-4. Intensity distributions are displayed in terms of raw data sets (circles), fitted gaussian and annular components and their sum. Note that the irradiance axis is scaled differently for each beam shape for better readability. b) Peak and beam radius percentage variations ( $\Delta I_{pk}$  and  $\Delta w_{86}$ ) around the focal plane. The depicted linear trends are only indicative. c) Melt pool aspect ratio (AR) as a function of  $I_{pk}/v$  ratio at various focal position for indices BS0-4 and vs  $I_r/v$  for index BS4. Note the logarithmic scale on the  $I_{pk}/v$  and  $I_r/v$  axis. Main trend lines are only indicative. Results belong to optical configuration 2.

better retains its radius and peak intensity. This is demonstrated by the percentage variations of peak intensity and beam radius, namely  $\Delta I_{pk}$  and  $\Delta w_{86}$ , of the two beam profiles at the tested focal positions, represented in Fig. 16b and defined as:

$$\begin{aligned} \Delta I_{pk}(\%) &= \frac{I_{pk}(\Delta z = 0) - I_{pk}(\Delta z = \pm 1.5)}{I_{pk}(\Delta z = 0)} * 100 \\ \Delta w_{86}(\%) &= \frac{w_{86}(\Delta z = \pm 1.5) - w_{86}(\Delta z = 0)}{w_{86}(\Delta z = 0)} * 100 \end{aligned} \quad (9)$$

Note that according to this definition (see Eq. (9)),  $\Delta I_{pk}$  refers to a percentage decrease as the maximum intensity peak is expected at the beam waist, while  $\Delta w_{86}$  refers to a percentage increase as the beam radius is expected to increase moving out of the focal plane.

Coherently, the fitted radii included in the models ( $w_G$ ,  $w_1$ ,  $w_{G2}$ ) and the coefficient of power partition ( $\alpha$ ) slightly increased outside the focal plane, indicating a shift in the intensity distribution towards a Gaussian profile. Table 2 in the Supplementary material shows the fitted model coefficients along with the maximum intensity and annular peaks of the tested beam profiles. The asymmetry of the irradiance profiles observed in Fig. 12a at the boundary of the acquisitions did not occur in the optical configuration 2. This different behaviour is attributed to the absence of the F-Theta lens, for which the paraxial approximation may not be applicable. The laser power drives the absolute value of the intensity distribution but is not expected to play a role in the beam profile and divergence. Focus shift induced by lens heating or nonlinear absorption triggered by highly intense beams can alter the beam propagation and the shape of the irradiance profiles but were not observed in the present study.

The individual effect of the model coefficients can be synthesized with two collective parameters, namely peak ( $I_{pk}$ ) and ring intensities ( $I_r$ ). With exception of the Gaussian distribution whose modeling cannot include an annular component, these values refer to the intensity peaks of a ring beam in correspondence of their origin ( $r = 0$ ) and the ring radius ( $r = w_1$ ). Under the assumption of  $w_1 > w_{G2}$ , to prevent the PDD to degenerate towards a Gaussian, and  $w_1 > w_G$ , the ring PDD ( $I_r$ ) of the torus model can be reduced to  $I_{pk}$  and  $I_r$  as follows:

$$\begin{aligned}
 I_{pk}(I_r(r = 0)) &= \frac{2P_{tot}\alpha}{\pi w_G^2} = f(\alpha, w_G) \\
 I_r(I_r(r = w_1)) &= \frac{\frac{3P_{tot}(1-\alpha)}{w_{G2}^2}}{\pi \left( e^{-3\left(\frac{w_1}{w_{G2}}\right)^2} + \sqrt{3}\pi \frac{w_1}{w_{G2}} \left( 1 + erf\left(\sqrt{3} \frac{w_1}{w_{G2}}\right) \right) \right)} \\
 &= f(\alpha, w_1, w_{G2})
 \end{aligned}
 \tag{10}$$

These expressions entail that under reasonable assumptions,  $I_{pk}$  and  $I_r$  are dominated by the Gaussian and the Torus components of the superimposed models, respectively. The assumption  $w_1 > w_G$  is not strictly necessary and has been introduced just to discriminate the effect of the Gaussian and the Torus components on the intensity peaks. However, as shown in Table 2 of the Supplementary material, both the assumptions held true for any ring beam.

$I_{pk}$  and  $I_r$  models gather the information coming from the model coefficients in two collective indicators. Therefore, their introduction allowed to validate the analytical models (in this case T + G model) by correlating them with experimental results. Accordingly, Fig. 16c illustrates melt pool aspect ratio AR as a function of  $I_{pk}/v$  ratio for both BS0 and BS4, and of  $I_r/v$  ratio only for BS4, as the Gaussian beam was not modeled with a ring beam. The AR dataset referred to the power level (200 W) at which the optical datasets of the beams were acquired.  $I_{pk}$  and  $I_r$  are normalized to the scan speed as AR was dominated by the scan speed as shown in Fig. 14. Hence, the  $I_{pk}/v$  and  $I_r/v$  ratios define completely any experimental condition as all the input parameters are gathered in a simple descriptor. Without this normalization all the AR data sharing the same  $I_{pk}$  or  $I_r$  (which means at a defined focus position  $\Delta z$ ) would arrange along vertical lines, complicating the pursue of correlations.

Data revealed an increasing trend regardless of the focus position and the beam profile. For BS0, a moderate increase of  $\alpha$  and  $w_G$  when moving out of the focal plane resulted in a decrease of  $I_{pk}$  as the quadratic effect of the Gaussian radius at the denominator dominated this descriptor (see Eq. (10)). Therefore, the AR curve at  $\Delta z = 0$  mm lies above the curves at  $\Delta z = \pm 1.5$  mm as a higher penetration depth is achieved at the same

scan speed. Similarly, for BS4, a moderate increase of  $\alpha$ ,  $w_G$ ,  $w_1$ ,  $w_{G2}$  when moving out of the focal plane resulted in a decrease of both  $I_{pk}$  and  $I_r$ . For  $I_r$  the quadratic effect of the half the torus width radius dominated this descriptor, as occurs with  $I_{pk}$  and  $w_G$ . However, the AR curve at  $\Delta z = 0$  mm was superimposed to the curves at  $\Delta z = \pm 1.5$  mm. The reason for this behaviour was likely linked to the combination of power level (200 W) and the smaller percentage variations of peak intensity and beam radius for the ring profile, as depicted in Fig. 16b. This trend could already be observed in Fig. 14c although at a higher power level (400 W) the effect of  $\Delta z$  on the melt pool morphology can be clearly discerned.

Overall, this works provided an analytical basis to decode the growing shape complexity of ring beam profiles through the introduction of new parameters. Despite the model complexity in terms of number of coefficients to be estimated,  $I_{pk}$  and  $I_r$  allowed to synthesize their effects and serve as systematic tools for benchmarking ring beam profiles provided by different laser sources, which may employ diverse beam shaping principles. This research also demonstrated that all the experimental effort in high-power laser applications, e.g. laser welding, cutting or LPBF, cannot exclude the optical characterization of the beam which serve as the radiography of the laser tool itself. Eventually, the research was conducted on the two-dimensional dataset (intensity, radii) extracted from the beam profiler and the assumption of rotational symmetry of the PDD. Future developments will involve the same analytical framework on the three-dimensional dataset.

## 6. Conclusions

The study presents a comprehensive investigation into the design and characterization of ring beam profiles using analytical models. A double-core fibre laser source with in-source beam shaping capabilities was utilized to generate different ring beams under two optical architectures. One configuration was entirely dedicated to beam imaging while the other was employed to both experimentation and beam imaging to validate the analytical models. Consistently, three analytical models, constructed as the sum of a Gaussian and an annular component, were proposed to reproduce and decode their structure. This paper highlights the importance of introducing new shape-encoding parameters and the effectiveness of different superimposed models in the reproduction of ring profiles along the propagation axis of the beam. Overall, the results can be summarized as follows:

- The utilization of novel ring beams laser processes requires rigorous shape parameters to accurately describe their structure. Analytical ring models with two or three radii could effectively synthesize their structure, with the resultant shape determined by the power partition between the Gaussian and annular components.
- The Torus and Multi-Gaussian models demonstrated the best fitting quality for describing ring-based beam profiles, while the TEM<sub>01\*</sub> model underperformed, especially with ring beams dominated by the annular components.
- Despite the high model accuracy, the ring beam models failed in the reconstruction of a simple TEM<sub>00</sub> profile due to the inaccurate or unfeasible fitted annular component that constitutes the ring beam. Instead, modeling with a Gaussian distribution allowed for maintaining high fitting accuracy while reducing the model complexity. This occurred also when trying to adapt the ring model at various focus position, where the shape of the beam could degenerate towards a Gaussian distribution. The results indicate that this metric should be considered to define the operative depth of field of ring beams.
- Under reasonable shape assumptions, two collective parameters gathering the effects of the estimated model coefficients could be introduced, namely the peak and ring intensities. These descriptors were found to be correlated with experimental data demonstrating that their introduction could help the comprehension of complex laser-matter interactions under non-Gaussian beams.

## Declaration of competing interest

The authors declare that they have no known competing financial interests or personal relationships that could have appeared to influence the work reported in this paper.

## Acknowledgements

The authors acknowledge the support of the Italian Ministry of University and Education (MIUR) through the National Plan of Recovery and Resilience (PNRR). The authors are thankful to nLIGHT Inc. and Optoprim Srl for the laser source used throughout the experimental activity. Raylase GmbH, Direct Machining Control and Gentec-EO are acknowledged for the technical support and the continuous development of the products used during the project.

## Appendix A. Supplementary data

Supplementary data to this article can be found online at <https://doi.org/10.1016/j.jmapro.2024.02.069>.

## References

- [1] Dong L, Samson B. Fiber lasers: basics, technology, and applications. 1st ed. CRC Press; 2016. <https://doi.org/10.1201/9781315370521>.
- [2] Shi W, Fang Q, Zhu X, Norwood RA, Peyghambarian N. Fiber lasers and their applications. *Appl Optics* 2014;53:6554. <https://doi.org/10.1364/ao.53.006554>.
- [3] Kratky A, Schuöcker D, Liedl G. Processing with kW fibre lasers: advantages and limits. In: XVII international symposium on gas flow, chemical lasers, and high-power lasers. vol. 7131. SPIE; 2008. 71311X. <https://doi.org/10.1117/12.816655>.
- [4] Canning J. Fibre lasers and related technologies. *Opt Lasers Eng* 2006;44:647–76. <https://doi.org/10.1016/j.optlaseng.2005.02.008>.
- [5] Kliner DA, Farrow RL, Lugo J, O'Dea B, Hawke R, Victor B, et al. Advanced metal processing enabled by fiber lasers with tunable beam properties. In: Proceedings of SPIE, SPIE-Intl Soc Optical Eng; 2022. p. 18. <https://doi.org/10.1117/12.2614728>.
- [6] Mohammadpour M, Wang L, Kong F, Kovacevic R. Adjustable ring mode and single beam fiber lasers: a performance comparison. *Manuf Lett* 2020;25:50–5. <https://doi.org/10.1016/j.mfglet.2020.07.003>.
- [7] Quintino L, Costa A, Miranda R, Yapp D, Kumar V, Kong CJ. Welding with high power fiber lasers - a preliminary study. *Mater Des* 2007;28:1231–7. <https://doi.org/10.1016/j.matdes.2006.01.009>.
- [8] Okunkova A, Volosova M, Peretyagin P, Vladimirov Y, Zhirnov I, Gusarov AV. Experimental approbation of selective laser melting of powders by the use of non-Gaussian power density distributions. In: *Phys Procedia*. vol. 56. Elsevier B.V.; 2014. p. 48–57. <https://doi.org/10.1016/j.phpro.2014.08.095>.
- [9] Loh LE, Liu ZH, Zhang DQ, Mapar M, Sing SL, Chua CK, et al. Selective laser melting of aluminium alloy using a uniform beam profile. *Virtual Phys Prototyp* 2014;9:11–6. <https://doi.org/10.1080/17452759.2013.869608>.
- [10] Laskin A, Volpp J, Laskin V, Nara T, Jung SR. Multispot optics for beam shaping of high-power single-mode and multimode lasers. *J Laser Appl* 2021;33:042046. <https://doi.org/10.2351/7.0000461>.
- [11] Bremer SJL, Luckabauer M, Römer G, willem RBE.. Laser intensity profile as a means to steer microstructure of deposited tracks in directed energy deposition. *Mater Des* 2023;227. <https://doi.org/10.1016/j.matdes.2023.111725>.
- [12] Grigoriev SN, Gusarov AV, Metel AS, Tarasova TV, Volosova MA, Okunkova AA, et al. Beam shaping in laser powder bed fusion: Péclet number and dynamic simulation. *Metals (Basel)* 2022;12. <https://doi.org/10.3390/met12050722>.
- [13] Umhofer U, Jäger E, Bischoff C. Refractive and diffractive laser beam shaping optics. *Laser Technik Journal* 2011;8:24–7. <https://doi.org/10.1002/latj.201190020>.
- [14] Volpp J, Laskin VV, Ostrun AB, Laskin AV. Beam shaping of focused radiation of multimode lasers. *SPIE-Intl Soc Optical Eng* 2018;5. <https://doi.org/10.1117/12.2287980>.
- [15] Mohammadpour M, Wang L, Kong F, Kovacevic R. Adjustable ring mode and single beam fiber lasers: a performance comparison. *Manuf Lett* 2020;25:50–5. <https://doi.org/10.1016/j.mfglet.2020.07.003>.
- [16] Matthews MJ, Roehling TT, Khairallah SA, Guss G, Wu SQ, Crumb MF, et al. Spatial modulation of laser sources for microstructural control of additively manufactured metals. In: *Procedia CIRP*. vol. 74. Elsevier B.V.; 2018. p. 607–10. <https://doi.org/10.1016/j.procir.2018.08.077>.
- [17] Laskin A, Laskin V. Freeform beam shaping for high-power multimode lasers. In: *Laser resonators, microresonators, and beam control XVI*. vol. 8960. SPIE; 2014. 89601P. <https://doi.org/10.1117/12.2037007>.
- [18] Caprio L, Demir AG, Previtali B. Understanding the effects of temporal waveform modulation of the laser emission power in laser powder bed fusion: part I - analytical modelling. *J Phys D Appl Phys* 2022;55. <https://doi.org/10.1088/1361-6463/ac984c>.
- [19] Caprio L, Demir AG, Previtali B. Understanding the effects of temporal waveform modulation of laser emission power in laser powder bed fusion: part II - experimental investigation. *J Phys D Appl Phys* 2022;55. <https://doi.org/10.1088/1361-6463/ac984d>.
- [20] D'Arcangelo S, Caprio L, Chesi D, Nociolini D, Corbinelli R, Previtali B, et al. Comprehensive benchmarking of laser welding technologies including novel beam shapes and wavelengths for e-drive copper hairpins. *Opt Laser Technol* 2024;169. <https://doi.org/10.1016/j.optlastec.2023.109964>.
- [21] Singh A, Caprio L, Previtali B, Demir AG. Processability of pure Cu by LPBF using a ns-pulsed green fiber laser. *Opt Laser Technol* 2022;154. <https://doi.org/10.1016/j.optlastec.2022.108310>.
- [22] Dickey FM, Lizotte TE. Laser beam shaping applications. 2nd ed. CRC Press; 2019.
- [23] Dickey FM. Laser beam shaping: theory and techniques. 2nd ed. CRC Press; 2018.
- [24] Zhirnov IV, Podrabinnik PA, Okunkova AA, Gusarov AV. Laser beam profiling: experimental study of its influence on single-track formation by selective laser melting. *Mech Ind* 2015;16. <https://doi.org/10.1051/meca/2015082>.
- [25] Okunkova AA, Peretyagin PY, Podrabinnik PA, Zhirnov IV, Gusarov AV. Development of laser beam modulation assets for the process productivity improvement of selective laser melting. In: *Procedia IUTAM*. vol. 23. Elsevier B.V.; 2017. p. 177–86. <https://doi.org/10.1016/j.piutam.2017.06.019>.
- [26] Metel AS, Stebulyanin MM, Fedorov SV, Okunkova AA. Power density distribution for laser additive manufacturing (SLM): potential, fundamentals and advanced applications. *Technologies (Basel)* 2019;7. <https://doi.org/10.3390/technologies7010005>.
- [27] Kang SG, Shin J. Laser beam oscillation welding of aluminum alloy using the spatially modulated beam by diffractive optical element (DOE). *J Manuf Process* 2021;66:387–96. <https://doi.org/10.1016/j.jmapro.2021.04.029>.
- [28] Wang L, Gao X, Kong F. Keyhole dynamic status and spatter behavior during welding of stainless steel with adjustable-ring mode laser beam. *J Manuf Process* 2022;74:201–19. <https://doi.org/10.1016/j.jmapro.2021.12.011>.
- [29] Maina MR, Okamoto Y, Okada A, Närhi M, Kangastupa J, Vihinen J. High surface quality welding of aluminum using adjustable ring-mode fiber laser. *J Mater Process Technol* 2018;258:180–8. <https://doi.org/10.1016/j.jmatprotec.2018.03.030>.
- [30] Möller M, Haug P, Scheible P, Buse C, Frischkorn C, Speker N. Spatially tailored laser energy distribution using innovative optics for gas-tight welding of casted and wrought aluminum alloys in e-mobility. *J Laser Appl* 2022;34:042015. <https://doi.org/10.2351/7.0000735>.
- [31] Pamarthi VV, Sun T, Das A, Franciosa P. Tailoring the weld microstructure to prevent solidification cracking in remote laser welding of AA6005 aluminium alloys using adjustable ringmode beam. *J Mater Res Technol* 2023;25:7154–68. <https://doi.org/10.1016/j.jmrt.2023.07.154>.
- [32] Jabar S, Baghbani Barenji A, Franciosa P, Kotadia HR, Ceglarek D. Effects of the adjustable ring-mode laser on intermetallic formation and mechanical properties of steel to aluminium laser welded lap joints. *Mater Des* 2023;227. <https://doi.org/10.1016/j.matdes.2023.111774>.
- [33] Prieto C, Vaamonde E, Diego-Vallejo D, Jimenez J, Urbach B, Vidne Y, et al. Dynamic laser beam shaping for laser aluminium welding in e-mobility applications. In: *Procedia CIRP*. vol. 94. Elsevier B.V.; 2020. p. 596–600. <https://doi.org/10.1016/j.procir.2020.09.084>.
- [34] Kardan M, Levichev N, Castagne S, Duflou JR. Dynamic beam shaping requirements for fiber laser cutting of thick plates. *J Manuf Process* 2023;103:287–97. <https://doi.org/10.1016/j.jmapro.2023.08.048>.
- [35] Horník P, Šebestová H, Novotný J, Mrňa L. Laser beam oscillation strategy for weld geometry variation. *J Manuf Process* 2022;84:216–22. <https://doi.org/10.1016/j.jmapro.2022.10.016>.
- [36] Cloots M, Uggowitz PJ, Wegener K. Investigations on the microstructure and crack formation of IN738LC samples processed by selective laser melting using Gaussian and doughnut profiles. *Mater Des* 2016;89:770–84. <https://doi.org/10.1016/j.matdes.2015.10.027>.
- [37] Tunkur TU, Voisin T, Shi R, Depond PJ, Roehling TT, Wu S, et al. Nondiffractive beam shaping for enhanced optothermal control in metal additive manufacturing. *Opt Lett* 2021. <https://doi.org/10.1126/sciadv.abg9358>.
- [38] Roehling TT, Shi R, Khairallah SA, Roehling JD, Guss GM, McKeown JT, et al. Controlling grain nucleation and morphology by laser beam shaping in metal additive manufacturing. *Mater Des* 2020;195. <https://doi.org/10.1016/j.matdes.2020.109071>.
- [39] Roehling TT, Wu SSQ, Khairallah SA, Roehling JD, Soezeri SS, Crumb MF, et al. Modulating laser intensity profile ellipticity for microstructural control during metal additive manufacturing. *Acta Mater* 2017;128:197–206. <https://doi.org/10.1016/j.actamat.2017.02.025>.
- [40] Shi R, Khairallah SA, Roehling TT, Heo TW, McKeown JT, Matthews MJ. Microstructural control in metal laser powder bed fusion additive manufacturing using laser beam shaping strategy. *Acta Mater* 2020;184:284–305. <https://doi.org/10.1016/j.actamat.2019.11.053>.
- [41] Wischeropp TM, Tarhini H, Emmelmann C. Influence of laser beam profile on the selective laser melting process of AISI10Mg. *J Laser Appl* 2020;32:022059. <https://doi.org/10.2351/7.0000100>.
- [42] Grünwald J, Gehringer F, Schmöller M, Wudy K. Influence of ring-shaped beam profiles on process stability and productivity in laser-based powder bed fusion of AISI 316L. *Metals (Basel)* 2021;11. <https://doi.org/10.3390/met11121989>.
- [43] Grünwald J, Bickler V, Allenberg-Rabe M, Wagenblast P, Wudy K. Flexible and highly dynamic beam shaping for Laser-Based Powder Bed Fusion of metals. In: *Procedia CIRP*. vol. 111. Elsevier B.V.; 2022. p. 65–70. <https://doi.org/10.1016/j.procir.2022.08.124>.
- [44] Grünwald J, Reimann J, Wudy K. Influence of ring-shaped beam profiles on spatter characteristics in laser-based powder bed fusion of metals. *J Laser Appl* 2023;35. <https://doi.org/10.2351/7.0001153>.

- [45] Galbusera F, Caprio L, Previtali B, Demir AG. The influence of novel beam shapes on melt pool shape and mechanical properties of LPBF produced Al-alloy. *J Manuf Process* 2023;85:1024–36. <https://doi.org/10.1016/j.jmapro.2022.12.007>.
- [46] Nahr F, Bartels D, Rothfelder R, Schmidt M. Influence of novel beam shapes on laser-based processing of high-strength aluminium alloys on the basis of EN AW-5083 single weld tracks. *J Manuf Mater Process* 2023;7:93. <https://doi.org/10.3390/jmmp7030093>.
- [47] Mohebbi MS, Ploshikhin V. Development of fully equiaxed microstructure in Scalmetal® through powder bed fusion using a ring-mode laser beam. *Scr Mater* 2023;236. <https://doi.org/10.1016/j.scriptamat.2023.115680>.
- [48] Rothfelder R, Huber F, Schmidt M. Influence of beam shape on spatter formation during PBF-LB/M of Ti6Al4V and tungsten powder. In: *Procedia CIRP*. vol. 111. Elsevier B.V.; 2022. p. 14–7. <https://doi.org/10.1016/j.procir.2022.08.105>.
- [49] Galbusera F, Caprio L, Previtali B, Demir AG. Tailoring the microstructure of Fe-2.9wt.%Si alloy in laser powder bed fusion using in-source beam shaping. *Opt Laser Technol* 2024;174:110649. <https://doi.org/10.1016/j.optlastec.2024.110649>.
- [50] Stuch J, Timpe NF, Scholl M, Russek UA. Localisation: characterisation of laser beam shape for materials processing using a new parameter. In: *High-power laser materials processing: lasers, beam delivery, diagnostics, and applications V*. vol. 9741. SPIE; 2016. 97410M. <https://doi.org/10.1117/12.2208648>.
- [51] Wu J, Ren S, Zhang Y, Cao Y, Zhang D, Yin C. Influence of spatial laser beam profiles on thermal-fluid transport during laser-based directed energy deposition. *Virtual Phys Prototyp* 2021;16:444–59. <https://doi.org/10.1080/17452759.2021.1960734>.
- [52] Goffin N, Tyrer JR, Jones LCR, Higginson RL. Simulated and experimental analysis of laser beam energy profiles to improve efficiency in wire-fed laser deposition. *Int J Adv Manuf Technol* 2021. <https://doi.org/10.1007/s00170-021-07029-y/Published>.
- [53] Promopattum P, Yao SC. Influence of scanning length and energy input on residual stress reduction in metal additive manufacturing: numerical and experimental studies. *J Manuf Process* 2020;49:247–59. <https://doi.org/10.1016/j.jmapro.2019.11.020>.
- [54] Shehryar Khan M, Shahabadi SI, Yavuz M, Duley WW, Biro E, Zhou Y. Numerical modelling and experimental validation of the effect of laser beam defocusing on process optimization during fiber laser welding of automotive press-hardened steels. *J Manuf Process* 2021;67:535–44. <https://doi.org/10.1016/j.jmapro.2021.05.006>.
- [55] Qiu Y, Niu X, Song T, Shen M, Li W, Xu W. Three-dimensional numerical simulation of selective laser melting process based on SPH method. *J Manuf Process* 2021;71:224–36. <https://doi.org/10.1016/j.jmapro.2021.09.018>.
- [56] Duocastella M, Arnold CB. Bessel and annular beams for materials processing. *Laser Photon Rev* 2012;6:607–21. <https://doi.org/10.1002/lpor.201100031>.
- [57] Zapata A, Zhao XF, Li S, Bernauer C, Zaeh MF. Three-dimensional annular heat source for the thermal simulation of coaxial laser metal deposition with wire. *J Laser Appl* 2023;35. <https://doi.org/10.2351/7.0000813>.
- [58] Vanmunster L, Goossens L, Kinds Y, Van Hooreweder B, Vrancken B. Effect of a variable laser beam profile system on productivity and surface quality of 316L stainless steel parts produced by Laser Powder Bed Fusion. *CIRP Annals* 2023. <https://doi.org/10.1016/j.cirp.2023.04.035>.
- [59] Holla V, Kopp P, Grünewald J, Wudy K, Kollmannsberger S. Laser beam shape optimization in powder bed fusion of metals. *Addit Manuf* 2023;72. <https://doi.org/10.1016/j.addma.2023.103609>.
- [60] Li Q, Luo M, Mu Z, Huang A, Pang S. Improving laser welding via decreasing central beam density with a hollow beam. *J Manuf Process* 2022;73:939–47. <https://doi.org/10.1016/j.jmapro.2021.12.001>.
- [61] Wu G, Lou Q, Zhou J, Dong J, Wei Y, Su Z. Propagation of flat-topped beams. *Opt Laser Technol* 2008;40:494–8. <https://doi.org/10.1016/j.optlastec.2007.08.001>.
- [62] Wang Z, Jiang M, Chen X, Du Y, Lei Z, Zhao S, et al. Mitigating spatters in keyhole-mode laser welding by superimposing additional ring-shaped beam. *Opt Laser Technol* 2024;168. <https://doi.org/10.1016/j.optlastec.2023.109869>.
- [63] Moore R, Orlandi G, Rodgers T, Moser D, Murdoch H, Abdeljawad F. Microstructure-based modeling of laser beam shaping during additive manufacturing. *JOM* 2024. <https://doi.org/10.1007/s11837-023-06363-8>.
- [64] Steen WM, Mazumder J. *Laser material processing*. London: Springer; 2010. <https://doi.org/10.1007/978-1-84996-062-5>.
- [65] Arlt J, Padgett MJ. Generation of a beam with a dark focus surrounded by regions of higher intensity: the optical bottle beam. vol. 25; 2000. <https://doi.org/10.1364/OL.25.000191>.
- [66] Chen G-Y, Song F, Wang H-T. Sharper focal spot generated by  $4\pi$  tight focusing of higher-order Laguerre–Gaussian radially polarized beam. *Opt Lett* 2013;38:3937. <https://doi.org/10.1364/ol.38.003937>.
- [67] Padgett MJ, Allen L, Allen JF. *The Poynting vector in Laguerre-Gaussian laser modes*. vol. 121; 1995.
- [68] Dholakia K, Simpson NB, Padgett MJ, Allen L. Second-harmonic generation and the orbital angular momentum of light. *Phys Rev A (Coll Park)* 1996;5:R3742–5. <https://doi.org/10.1103/PhysRevA.54.R3742>.
- [69] Meschede D. *Optics, light, and lasers: the practical approach to modern aspects of photonics and laser physics*. 2nd ed. Wiley-VCH; 2007.
- [70] Wang L, Mohammadpour M, Gao X, Lavoie JP, Kleine K, Kong F, et al. Adjustable Ring Mode (ARM) laser welding of stainless steels. *Opt Lasers Eng* 2021;137. <https://doi.org/10.1016/j.optlaseng.2020.106360>.
- [71] Wang L, Demir AG, Previtali B. Observing molten pool surface oscillations during keyhole processing in laser powder bed fusion as a novel method to estimate the penetration depth. *Addit Manuf* 2020;36. <https://doi.org/10.1016/j.addma.2020.101470>.
- [72] Caprio L, Demir AG, Previtali B. External illumination enables coaxial sensing of surface and subsurface molten pool geometry in LPBF. *Metals (Basel)* 2022;12. <https://doi.org/10.3390/met12101762>.
- [73] Reitemeyer D, Seefeld T, Vollertsen F. Online focus shift measurement in high power fiber laser welding. In: *Phys Procedia*. vol. 5. Elsevier B.V.; 2010. p. 455–63. <https://doi.org/10.1016/j.phpro.2010.08.073>.
- [74] Vogt S, Völl A, Wollgarten S, Freese T, Stollenwerk J, Weisheit A, et al. Local laser softening of high-strength steel with an adapted intensity. *J Laser Appl* 2019;31. <https://doi.org/10.2351/1.5052147>.
- [75] Meunier M, Cornee R, Lucas A, Lemaitre D, Vernaz-Gris P, Pallier G, et al. Fully reflective annular laser beam shaping for laser beam welding at 16kW. n.d.
- [76] Huang Y Jun, Xie X Zhu, Cui J Qi, Long J You. Fabrication of high-performance copper circuits using laser-induced forward transfer with large receiving gaps based on beam modulation technology. *J Manuf Process* 2023;87:54–64. <https://doi.org/10.1016/j.jmapro.2022.12.061>.
- [77] Tenbrock C, Fischer FG, Wissenbach K, Schleifenbaum JH, Wagenblast P, Meiners W, et al. Influence of keyhole and conduction mode melting for top-hat shaped beam profiles in laser powder bed fusion. *J Mater Process Technol* 2020; 278. <https://doi.org/10.1016/j.jmatprotec.2019.116514>.
- [78] King WE, Barth HD, Castillo VM, Gallegos GF, Gibbs JW, Hahn DE, et al. Observation of keyhole-mode laser melting in laser powder-bed fusion additive manufacturing. *J Mater Process Technol* 2014;214:2915–25. <https://doi.org/10.1016/j.jmatprotec.2014.06.005>.
- [79] Cunningham R, Zhao C, Parab N, Kantzos C, Pauza J, Fezzaa K, et al. Keyhole threshold and morphology in laser melting revealed by ultrahigh-speed x-ray imaging downloaded from vol. 363; 2019. <https://doi.org/10.1126/science.aav4687>.
- [80] Calta NP, Wang J, Kiss AM, Martin AA, Depond PJ, Guss GM, et al. An instrument for in situ time-resolved X-ray imaging and diffraction of laser powder bed fusion additive manufacturing processes. *Rev Sci Instrum* 2018;89. <https://doi.org/10.1063/1.5017236>.
- [81] Parab ND, Zhao C, Cunningham R, Escano LI, Fezzaa K, Everhart W, et al. Ultrafast X-ray imaging of laser–metal additive manufacturing processes. *J Synchrotron Radiat* 2018;25:1467–77. <https://doi.org/10.1107/S1600577518009554>.